Deterministic single-photon source over the terahertz regime

Caspar Groiseau [1,2,3,*] Miguel Á. Martínez-García [2,3] Diego Martín-Cano [2,3,4,†] and Carlos Sánchez Muñoz [5,6,‡]

[1]*Department of Microtechnology and Nanoscience, Chalmers University of Technology, 412 96 Gothenburg, Sweden*
[2]*Departamento de Físíca Teórica de la Materia Condensada, Universidad Autónoma de Madrid, 28049 Madrid, Spain*
[3]*Condensed Matter Physics Center (IFIMAC), Universidad Autónoma de Madrid, 28049 Madrid, Spain*
[4]*Instituto Nicolás Cabrera, Universidad Autónoma de Madrid, 28049 Madrid, Spain*
[5]*Quantum Advanced Research Center (QuARC), CSIC, Calle Serrano 113b, 28006 Madrid, Spain*
[6]*Institute of Fundamental Physics IFF-CSIC, Calle Serrano 113b, 28006 Madrid, Spain*

(Received 16 October 2025; accepted 13 October 2026; published 16 November 2026)

The terahertz (THz) regime still lacks a source capable of emitting single photons deterministically. Here, we propose an on-demand THz single-photon source, triggered by a sequence of coherent optical pulses used to dress a polar quantum emitter. The permanent dipole moment of the emitter activates THz transitions within its Rabi-split doublets, which are enhanced through resonant coupling to a THz cavity. We identify a challenge unique to this platform: Spontaneous emission of visible photons competes with the THz process, degrading performance in two distinct ways depending on the sign of the drive detuning—either increasing the vacuum component, reducing brightness, or increasing multiphoton contributions, reducing purity. We demonstrate how to overcome those challenges through optimized pulse areas and a sufficiently high Purcell rate. A hybrid resonator-nanoparticle design for a cavity satisfying the latter requirement is presented, yielding efficiencies of 65%–92% and purities of 88%–100%, comparable to the best visible single-photon sources, while providing broad tunability across the THz range. Finally, we exploit the visible emission itself, using its detection to fully reconstruct the THz photon-number distribution and herald a single THz photon, boosting efficiency to 90%–95%. All these capabilities illustrate the new technological opportunities unlocked by the unique integration of terahertz and visible frequencies.

DOI: 10.1103/hpwn-ld2q

I. INTRODUCTION

Single-photon emitters (SPEs) are essential building blocks for the generation of nonclassical correlations involved in light-based quantum technologies [1–3]. To perform useful quantum protocols, SPEs are required to fulfill bright and efficient emission properties, and the ability to trigger on demand indistinguishable single photons with a well-defined spatiotemporal mode. These demands have led to a contest to integrate a plethora of different solid-state emitters in various nanophotonic platforms, including quantum dots [4], single defects [2], superconducting qubits [5], and molecules [6], with the prospects of becoming standard sources for quantum optical technologies.

While the race for SPEs began long ago for visible and microwave wavelengths, it has just begun for terahertz (THz) radiation (0.1–70 THz) [7]. The THz is among the latest exploited gaps in the electromagnetic spectrum, with broad applications in communications, biology, medicine, spectroscopy, and materials characterization [7,8]. The historical delay in the development of classical THz technology, together with the absence of bright and efficient photonic transitions at THz frequencies [9]—naturally occurring in molecules, superconducting junctions, or semiconductors—have prevented any experimental findings of THz SPEs. Only a few proposals of heralded THz photon sources exist, such as spontaneous parametric down-conversion experiments [10] and polariton optomechanical mechanisms in the midinfrared [11–13]. Developing such THz SPEs would set an alternative quantum optical platform offering a compromise between the challenges of the visible (nanometric tolerance requirements) and microwave spectrum (scalability, mK cooling).

A promising approach for generating THz radiation involves leveraging the interaction between cavities and laser-dressed electronic transitions in polar systems [14–19]. Permanent dipole moments in asymmetric emitters enable nonlinear radiative transitions between laser-dressed states of the same Rabi doublet, which can achieve THz frequencies. In a recent work [20], we have shown that Purcell enhancement of this mechanism by THz cavities allows one to generate a continuous THz SPE, which bypasses the large ratio between dephasing and transition rates that hinder conventional optical dipole transitions at THz frequencies [21]. However, continuous SPEs do not allow deterministic timing of photon emission events and result in emission over steady-state mixtures within finite detection windows, limiting indistinguishability and compatibility with synchronized quantum protocols.

*Contact author: groiseau@chalmers.se
†Contact author: diego.martin.cano@uam.es
‡Contact author: carlos.sanchez@iff.csic.es

Published by the American Physical Society under the terms of the Creative Commons Attribution 4.0 International license. Further distribution of this work must maintain attribution to the author(s) and the published article's title, journal citation, and DOI. Funded by Bibsam.

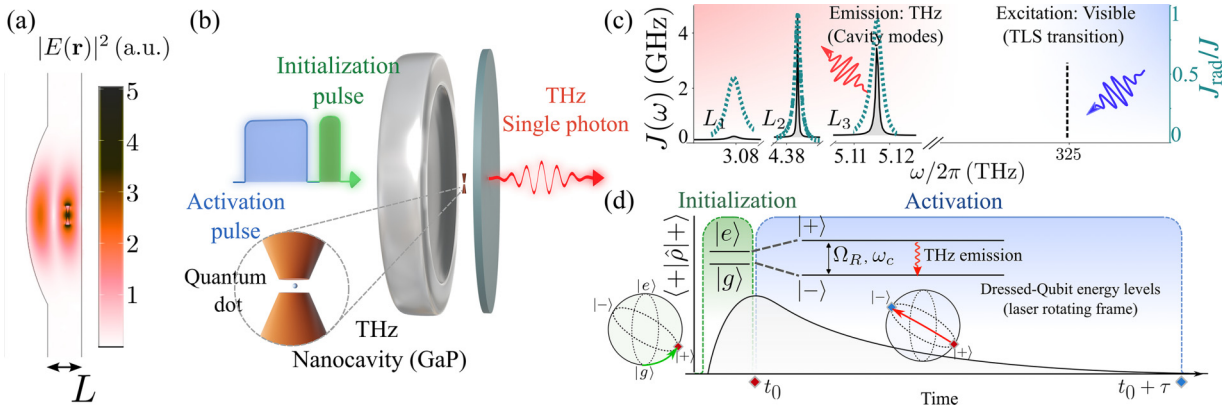


FIG. 1. (a) Electric field cross-section simulation and sketch [panel (b)] of a potential experimental implementation of a deterministic single-photon THz source consisting of a quantum emitter held in a hybrid nanocavity made up by two GaP nanocones (length 11.07 μm, tip radius 0.39 μm, and bottom radius 2.37 μm) separated by 50 nm, both embedded within a Fabry-Pérot resonator that is triggered by the initialization and activation pulse protocols in the visible (green and blue areas). (c) Simulations of the spectral density J and its radiative part $J_{\rm rad}$ of three different frequency-detuned hybrid cavities with lengths $\{L_1, L_2, L_3\} = \{108.9\ \mu\text{m}, 74.7\ \mu\text{m}, 63.4\ \mu\text{m}\}$. (d) Temporal evolution of the population of $|+\rangle$ during the first two pulses, including trajectory on the Bloch sphere.

Here, we develop a full scheme for on-demand, optically heralded generation of single photons in the THz regime with high purity, efficiency, and indistinguishability. We realize this by combining a tailored pulse protocol with a feasible hybrid-cavity design [see Figs. 1(a) and 1(b)]. While competing visible-photon emission can degrade the output purity, its impact can be minimized through optimized cavity and pulse design. At the same time, these visible photons enable heralding and complete tomographic reconstruction of the photon-number distribution of the emitted THz state using fully optical detection.

II. SYSTEM AND MODEL

We use a single optical polar quantum emitter described as a two-level system (TLS) with ground state $|g\rangle$ and excited state $|e\rangle$, separated by the optical transition frequency ω_0. The TLS interacts with a single THz cavity mode represented by the annihilation operator $\hat{a}$, characterized by the THz frequency ω_c and the associated field $\mathbf{E}_c$. In our proposal, this mode is realized through a hybrid-cavity structure consisting of a Fabry-Pérot resonator coupled to a THz nanocavity formed by two separated GaP nanocones, as illustrated in Figs. 1(a) and 1(b). These structures, as well as the required emitter positioning, are within the capabilities of current fabrication technologies [22,23], the cones being supported either by tips or by ultralow-refractive-index substrates, which have already been successfully employed in THz microcavity implementations [24,25]. We perform full electromagnetic dipole simulations [26] to estimate the photonic spectral local density at the center of the nanocavity at THz frequencies [see Fig. 1(c)]. This hybrid architecture enables broadband tunability of the THz emission by leveraging the external control of the cavity length L—see different mode spectral densities in Fig. 1(c) for varying L—together with the flat response of GaP at frequencies well below phonon polariton resonances [27]. These cavity modes enable a 10^6-fold emission enhancement with respect to free space and high radiative efficiency, due to the high refractive index of the semiconductor material [27] in combination with the finesse of the Fabry-Pérot resonator [28]. Finally, the TLS is driven by an optical laser field $\mathbf{E}_L$ with frequency ω_L.

This system is described through the Hamiltonian ($\hbar = 1$ henceforth)

$$\hat{H} = \omega_0\hat{\sigma}_z/2 + \omega_c\hat{a}^\dagger\hat{a} + \hat{\mathbf{d}}\cdot\mathbf{E}_c(\hat{a}+\hat{a}^\dagger) + \hat{\mathbf{d}}\cdot\mathbf{E}_L\cos(\omega_L t), \tag{1}$$

where the dipole operator $\hat{\mathbf{d}}$ is defined as $\hat{\mathbf{d}} = \mathbf{d}_{ee}(1+\hat{\sigma}_z)/2 + \mathbf{d}_{ge}(\hat{\sigma}_+ + \hat{\sigma}_-)$, $\hat{\sigma}_\pm$ being the raising and lowering operators of the TLS. The term $\propto \mathbf{d}_{ee}$ accounts for the permanent dipole component due to the asymmetric charge distribution of the polar emitter. After moving to the laser rotating frame and eliminating all terms oscillating with visible frequencies [20], the optical coherent drive yields two dressed eigenstates $|\pm\rangle$ within the TLS-laser system [see Fig. 1(d)], split by the generalized Rabi frequency $\Omega_R = \sqrt{\Delta^2+\Omega^2}$, where $\Delta = \omega_L - \omega_0$ represents the laser detuning and $\Omega = \mathbf{d}_{ge}\cdot\mathbf{E}_L$ denotes the driving amplitude [17,29]. These dressed states, $|+\rangle = s|e\rangle + c|g\rangle$ and $|-\rangle = s|g\rangle - c|e\rangle$, are defined by $s \equiv \sin\theta$, $c \equiv \cos\theta$, where $\theta \equiv \arctan[h^{\mathrm{sgn}(\Delta)}] \in [0, \frac{\pi}{4}]$, and where

$$h \equiv \frac{\Omega_R - |\Delta|}{\Omega} \in [0,1], \tag{2}$$

which we term dressing ratio, characterizes the crossover from the undressed regime ($h = 0$) to the fully dressed regime of resonant driving ($h = 1$). The operators $\hat{\sigma}_{\pm,z}$ are straightforwardly expressed using the Pauli matrices of the dressed-state basis, denoted as $\hat{\zeta}_\pm \equiv |\pm\rangle\langle\mp|$ and $\hat{\zeta}_z \equiv |+\rangle\langle+| - |-\rangle\langle-|$ [30]. In the dressed basis, the resulting Hamiltonian reads

$$\hat{H} = \frac{\Omega_R}{2}\hat{\zeta}_z + \omega_c\hat{a}^\dagger\hat{a} + \chi(\hat{a}+\hat{a}^\dagger)[1+(s^2-c^2)\hat{\zeta}_z] - 2cs\chi(\hat{a}\hat{\zeta}_- + \hat{a}^\dagger\hat{\zeta}_+) - 2cs\chi(\hat{a}\hat{\zeta}_+ + \hat{a}^\dagger\hat{\zeta}_-), \tag{3}$$

where $\chi = \mathbf{d}_{ee}\cdot\mathbf{E}_c/2$ is the coupling rate between the TLS and the THz cavity.

Additionally, we describe cavity decay and TLS spontaneous emission at optical frequencies with rates κ and γ,

respectively. The full open quantum system used in our simulations is thus given by the master equation

$$\mathcal{L}\hat{\rho} \equiv \partial_t \hat{\rho} = -i[\hat{H}, \hat{\rho}] + \frac{\kappa}{2}\mathcal{D}(\hat{X})\hat{\rho} + \frac{1}{2}\mathcal{D}(-\sqrt{\gamma_+}\hat{\xi}_+ + \sqrt{\gamma_-}\hat{\xi}_- + \sqrt{\gamma_z}\hat{\xi}_z)\hat{\rho}, \quad (4)$$

where $\gamma_- = \gamma s^4$, $\gamma_+ = \gamma c^4$, $\gamma_z = \gamma c^2 s^2$, $\mathcal{L}$ is the Liouvillian superoperator, and $\mathcal{D}(\hat{O})\hat{\rho} = 2\hat{O}\hat{\rho}\hat{O}^\dagger - \hat{O}^\dagger\hat{O}\hat{\rho} - \hat{\rho}\hat{O}^\dagger\hat{O}$ is the Lindblad superoperator. The cavity decay is described by the operator $\hat{X} = \sum_{j,k>j}\sqrt{\frac{\omega_k-\omega_j}{\omega_c}}\langle j|(\hat{a}+\hat{a}^\dagger)|k\rangle|j\rangle\langle k|$, which accounts for the counterrotating terms required beyond the secular approximation [20,31]. Here, $|k\rangle$ is the kth eigenstate with energy ω_k.

Under the resonant condition $\omega_c = \Omega_R$, and provided $\chi \ll \omega_c$, we can eliminate terms oscillating at THz frequencies and get a Jaynes-Cummings Hamiltonian $\hat{H}_{\rm JC} = g(\hat{a}\hat{\xi}_+ + \hat{a}^\dagger\hat{\xi}_-)$ [17,20], where we have defined the effective coupling strength $g = -2cs\chi$. Two further approximations will allow us to obtain analytical results: (1) First, we assume that we are in the far-off-resonant regime ($|\Delta| \gg \Omega$). This implies that $h \ll 1$, allowing us to set $\gamma_\mp = \gamma_z \approx 0$ and $\gamma_\pm = \gamma$, where from now on we refer the upper and lower subindexes to $\Delta > 0$ and $\Delta < 0$, respectively. (2) Second, we assume an irreversible, dissipative coupling to the cavity, which can be eliminated under the condition $\kappa \gg \gamma, g$. Using standard adiabatic elimination techniques [32], we obtain

$$\mathcal{L}_{\rm adb}\,\hat{\rho} \equiv \frac{\gamma_\pm}{2}\mathcal{D}(\hat{\xi}_\pm)\hat{\rho} + \frac{\Gamma}{2}\mathcal{D}(\hat{\xi}_-)\hat{\rho}, \quad (5)$$

where $\Gamma \equiv 4g^2/\kappa$ is the effective Purcell rate associated with the characteristic timescale for the emission of a THz photon through the cavity [33]. We are left with two competing processes: the desired decay through the cavity with rate Γ and a detrimental incoherent pump/decay with rate $\gamma_\pm$.

III. PROTOCOL

The deterministic protocol consists of two consecutive optical laser pulses [see Figs. 1(b) and 1(d)] that are applied sequentially to the ground state of the TLS-cavity system, $\hat{\rho}(0) = |g\rangle\langle g| \otimes |0\rangle\langle 0|_{\rm THz}$ (both pulses have square shape). (1) First, a short initialization pulse prepares the system at time t_0 in a coherent superposition $\hat{\rho}(t_0) = |+\rangle\langle +| \otimes |0\rangle\langle 0|_{\rm THz}$, where $|+\rangle$ is the dressed excited state defined for a chosen angle θ. This state is prepared by a rotation of angle θ around the y axis, $\hat{U}_1 = \exp[i\hat{\sigma}_y\theta]$, which can be implemented using a drive with Hamiltonian $\hat{H}_1 = i\Omega_1(\hat{\sigma} - \hat{\sigma}^\dagger)$ applied for a duration $t_0 = \theta/\Omega_1$ (alternatively, any pulse shape with the same area and phase—e.g., a Gaussian—can be used). (2) Second, a long activation pulse $\hat{H}_d = \Omega(\hat{\sigma} + \hat{\sigma}^\dagger)/2$, of duration τ, dresses the system, creating Rabi doublets with THz splittings that couple resonantly with the cavity, $\Omega_R = \omega_c$. This induces a Purcell-enhanced radiative decay from $|+\rangle$ to $|-\rangle$ with rate Γ via the emission of a THz photon [see Fig. 1(d)].

IV. SPE FIGURES OF MERIT

In an ideal deterministic SPE, the probability P_1 of emitting exactly one photon per excitation cycle—commonly referred to as the brightness or *efficiency* of the source [34,35]—is equal to unity. We thus define $P_1(\tau)$ as the probability that the state $\hat{\rho}_0$ evolves over a time interval τ while emitting exactly one photon. This is given by

$$P_1(\tau) = \int_0^\tau \mathrm{Tr}(S_{\tau-t}\mathcal{K}S_t\hat{\rho}_0)dt, \quad (6)$$

where $\mathcal{K}\hat{\rho} \equiv \kappa\hat{X}\hat{\rho}\hat{X}^\dagger$ is the superoperator describing the quantum collapse after photon detection and $S_t = e^{(\mathcal{L}-\mathcal{K})t}$ is the conditional propagator for a time period t conditioned to no photodetection.

A single-photon source is also characterized by the indistinguishability and the purity [34,35]. The indistinguishability I—formally defined in Appendix A—quantifies to what degree different single-photon pulses share the same wavefunction, which is verified via Hong-Ou-Mandel interferometry. The purity $\Pi = 1 - g^{(2)}(0)$ informs about the likelihood of multiple photons being in the pulse, as established by the degree of quantum second-order coherence $g^{(2)}(0)$ measured in a Hanbury Brown-Twiss (HBT) setup. In this system, I and Π take essentially the same value.

Figures 2(a)–2(d) present exact results of efficiency P_1 versus activation pulse length τ. The two columns correspond to red and blue detuning, respectively, with the same absolute value of detuning. The two rows correspond to two distinct cavity lengths ($L_1 \approx 108.9$ μm and $L_3 \approx 63.4$ μm; see corresponding parameters in Table I), highlighting the straightforward tunability of the source via simple modifications of the cavity geometry. These results establish the crucial role of the drive detuning sign. A red-detuned drive stabilizes the maximum possible P_1 for any time $\tau \gg 1/\Gamma$ long enough to enable the cavity-mediated emission. In contrast, blue detuning requires an optimal pulse duration: Excessively long pulses degrade the purity by introducing higher-photon-number components through effective repumping induced by spontaneous emission of visible photons at rate γ.

To obtain further insights, we now derive approximate analytical expressions from the effective TLS model given by $\mathcal{L}_{\rm adb}$. Starting with the initial state $\hat{\rho}_0 = |+\rangle\langle +|$ set by the first pulse, we can straightforwardly compute $P_1(\tau)$ as

$$P_1(\tau) = \begin{cases} \frac{e^{-\gamma\tau} - e^{-\Gamma\tau}[1+\gamma\tau(1-1/\tilde{C})]}{(1-1/\tilde{C})^2}, & \Delta > 0, \\ \frac{\tilde{C}}{\tilde{C}+1}[1 - e^{-\tau(\gamma+\Gamma)}], & \Delta < 0. \end{cases} \quad (7)$$

Here, we introduced the effective cooperativity

$$\tilde{C} \equiv 4g^2/[\kappa(\gamma_- + \gamma_+)] = 4C/(h^2 + h^{-2}) \approx 4h^2C, \quad (8)$$

a version of the standard cooperativity $C = 4\chi^2/\kappa\gamma$, scaled by the factor h to account for the dependence of the coupling rate on the dressing. In the case $\Delta > 0$ and for $\tilde{C} \gg 1$, the optimum pulse duration $\tau_{\rm max}$ maximizing P_1 is given by $\tau_{\rm max} \simeq \Gamma^{-1}\ln\tilde{C}$, yielding a maximum probability $P_{\rm max} \simeq 1 - \ln\tilde{C}/\tilde{C}$. In this limit, the single-photon purity can be estimated to be $\Pi(\tau_{\rm max}) = 1 - 2\ln\tilde{C}/\tilde{C}$. For $\Delta < 0$, we can simply estimate $P_{\rm max} \simeq \tilde{C}/(\tilde{C}+1)$, to which the system relaxes on a timescale $\tau_{\rm rel} \sim (\Gamma + \gamma)^{-1}$ and $\Pi \simeq I \simeq 1$.

We see in Figs. 2(c) and 2(d) that Eq. (7) agrees well with the exact numerical results in a regime in which all of our assumptions are met. Interestingly, a configuration with cavity length L_3 [Figs. 2(a) and 2(b)] features a small decay rate κ that does not meet the requirements of strong dissipation

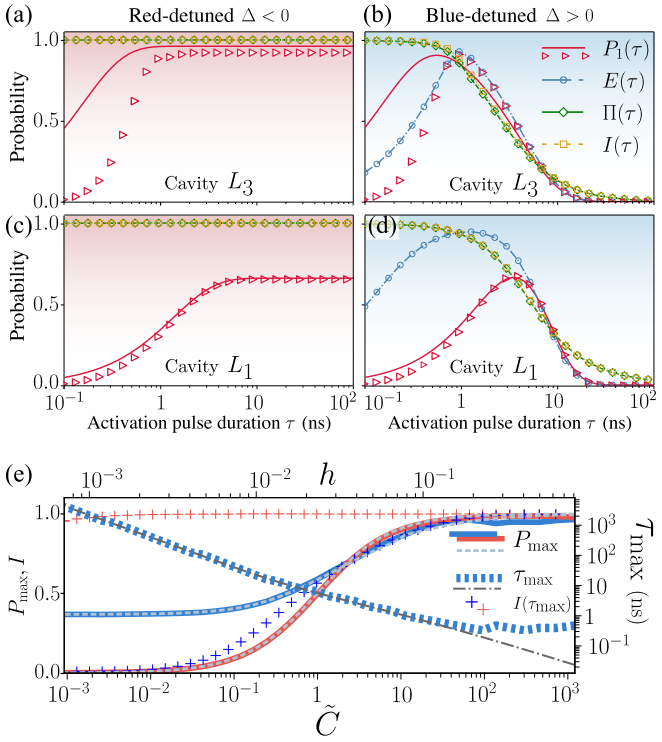


FIG. 2. (a)–(d) $P_1(\tau)$ obtained numerically (solid red) and analytically via Eq. (7) (red triangles); heralding efficiency $E(\tau)$ (blue circles); and purity $\Pi(\tau)$ (green diamonds) and indistinguishability $I(\tau)$ (yellow squares) vs activation pulse time τ. Results shown for cavity with length $L_3 = 63.4\,\mu$m [panels (a) and (b)] and $L_1 = 108.9\,\mu$m [panels (c) and (d)]. Parameters: $\Omega/2\pi = 0.2$ THz, corresponding to $h = 0.019\,55$ and $\tilde{C} = 24.65$ for cavity L_3, and $h = 0.0325$ and $\tilde{C} = 1.94$ for cavity L_1. (e) Results for cavity length L_1 for the maximum single-photon detection probability P_{max} (solid red and blue, for red and blue detuning, respectively); optimal activation pulse duration τ_{max} for the blue-detuned case (dashed blue), and their corresponding analytical estimates (dashed black for P_{max} and dash-dotted black for τ_{max}); and indistinguishability $I(\tau_{max})$ (blue and red crosses, for red and blue detuning, respectively), plotted as functions of the effective cooperativity $\tilde{C}$, varied via the detuning Δ, which effectively modifies the dressing ratio h (upper axis).

$\kappa \gg g$. Nevertheless, the source operates as an efficient SPE, with shorter τ_{max} and higher $P_{max} \approx 0.9$. This highlights that, although the conditions used to derive $\mathcal{L}_{adb}$ allow us to draw useful insights, they are not strictly necessary to achieve high-performance SPE operation.

Figure 2(e) shows the dependence of P_{max} and τ_{max} as a function of h for a cavity length L_1 (using the full model given by $\mathcal{L}$). These results indicate that the source performance is governed by $\tilde{C}$, via the bare cooperativity C and the dressing ratio h, suggesting that maximizing efficiency and minimizing τ_{max} benefits from working in the near-resonant regime $h \approx 1$ and large $\tilde{C}$. However, near-resonant driving entails some complications that make this a challenging regime of operation, such as larger required values of Ω in the THz range and a more important role of the decay terms $\gamma_{\mp}$ ignored in our analytics. Furthermore, highly blue-detuned regimes provide the advantage of working with an initial state very close to the bare ground state, $\hat{\rho}_0 = |+\rangle\langle+| \approx |g\rangle\langle g|$, making the initialization pulse unnecessary (see Appendix D). In conclusion, a compromise between large enough P_{max} and small enough h is desirable, such as the region $h \sim 0.1$ in the case shown in Fig. 2(e).

TABLE I. Parameters for two cavity configurations obtained by full electromagnetic dipole simulations.

	$\omega_c/2\pi$	$\chi/2\pi$	$\kappa/2\pi$	C	$\tilde{C}$
Cavity L_1	3.08 THz	4 GHz	3.5 GHz	460	1.94
Cavity L_3	5.12 THz	12.5 GHz	0.97 GHz	16 200	24.65

Regarding indistinguishability and purity, which are computed at τ_{max} ($\Delta > 0$) and $3\tau_{rel}$ ($\Delta < 0$), our numerics show that, for $\Delta < 0$, they always remain close to the maximum possible value, $I \approx \Pi \approx 1$. For $\Delta > 0$, they decreases with $\tilde{C}$ as the optimum pulse duration increases. In that case, a pulse duration shorter than the theoretical optimum is a more sensible choice, since it can maximize the heralding efficiency that we introduce below.

V. OPTICAL HERALDING AND TOMOGRAPHY

Up to this point, a blue-detuned configuration seemed to be the least favorable choice, as the repumping of the dressed TLS due to spontaneous emission in the visible leads to degradation of the quality of the SPE and requires pulse optimization. However, this configuration also allows one to use the detection of these visible photons to herald the THz SPE and even reconstruct its full photon-number distribution.

The key observation is that the state of the dressed emitter must be $|-\rangle$ following the emission of a THz photon, which for large blue detuning ($h \ll 1$ and $\Delta > 0$), approximates the bare excited state $|-\rangle \approx |e\rangle$. This state can subsequently relax via spontaneous emission of a visible photon in a timescale $1/\gamma$ [e.g., the first two emission events in the individual quantum trajectory depicted in Fig. 3(a)]. We can improve the protocol to work for an arbitrary h by applying a heralding pulse implementing the rotation $\hat{U} = \exp(-i\theta\hat{\sigma}_y)$ just after the activation pulse, which transforms the emitter as $|\pm\rangle \rightarrow |g/e\rangle$ and enables the optical decay conditioned on the prior emission of a THz photon.

The protocol can establish a near-perfect correlation between the number of photons emitted in the THz and visible regimes, as shown in Figs. 3(b) and 3(c). This correlation enables accurate reconstruction of the photon-number distribution $p(n)$ of the emitted THz state directly from optical measurements of its visible counterpart. If the photon-number resolution necessary to reconstruct $p(n)$ in the visible is not accessible, the protocol still allows one to herald a single THz photon emitted during the activation pulse interval $t \in (0, \tau)$, by the detection of an optical photon emitted after the pulse, i.e., at $t > \tau$. To quantify the efficiency of this heralded emission process, we define the corresponding conditional probability $E \equiv P(\text{THz}_{<\tau}|\text{optical}_{>\tau})$ (details on the calculation are provided in Appendixes G and H). The result is shown as blue circles in Figs. 2(b) and 2(d), indicating that this heralding protocol yields high efficiency $E \sim 0.92$–0.95, provided that the activation pulse duration is much longer than the cavity-photon lifetime $\tau \gg \kappa^{-1}$ and does not exceed

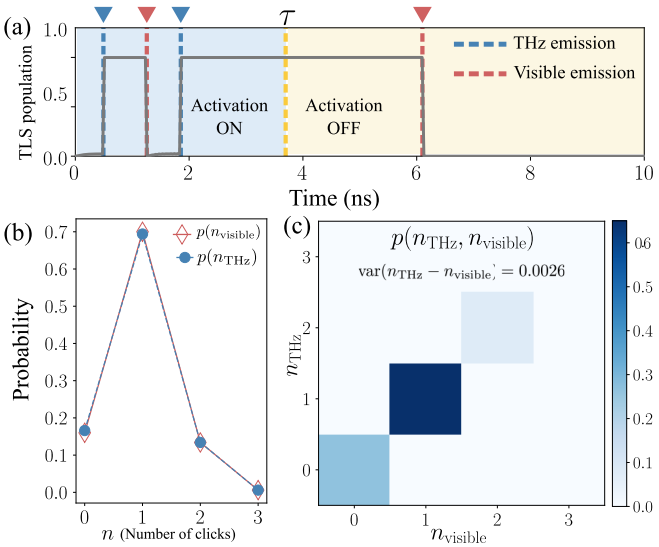


FIG. 3. Optical heralding and tomography for cavity L_1, $h = 0.0325$, and activation pulse length $\tau = \tau_{\max}$. (a) Single quantum trajectory in terms of the bare TLS population $\langle\hat{\sigma}_+\hat{\sigma}_-\rangle$ during the activation pulse (blue background), and the undriven evolution thereafter (yellow background). THz and visible-photon emission events are marked, illustrating the one-to-one correspondence between the total numbers of clicks. (b) Probability distribution of the number of emitted photons in the THz (n_{THz}) and the visible (n_{visible})—integrated over 30 ns after initialization pulse—showing that both distributions match (due to the large detuning used, no heralding pulse is necessary). (c) Joint probability distribution $p(n_{\text{THz}}, n_{\text{visible}})$, showing close to perfect correlation between both quantities as summarized by the negligible $\text{var}(n_{\text{THz}} - n_{\text{visible}})$.

$\tau_{\max}$. This latter upper limit arises since this simpler heralding does not discriminate between single- and multi-THz-photon emission, and therefore the heralding efficiency is degraded by optical repumping for $\tau > \tau_{\max}$ in the same way it degrades $P_1(\tau)$.

Optical heralding allows the use of shorter activation pulses to improve purity at the expense of brightness, enabling near-perfect heralded single-photon emission even when the intrinsic limit $P_{\max}$ is constrained. See Fig. 2(d), where $\max(E) \approx 0.95 \gg P_{\max}$ and I reaches 91%. This technique provides no advantage for red detuning ($\Delta < 0$), where the heralding efficiency is limited by the single-photon probability, i.e., $E(\tau) \approx P_1(\tau)$ for $\tau \gg (\gamma + \Gamma)^{-1}$.

VI. EXPERIMENTAL FEASIBILITY

Unlike ensemble-based lasing setups [17], which benefit from a collective enhancement of the light-matter interaction, the present proposal relies entirely on optimizing the single-emitter cooperativity $\tilde{C}$ through a careful choice of cavity parameters (influencing χ and κ), permanent dipole moment (influencing χ), and optical transition dipole moment (influencing γ). For the permanent dipole moment, we have taken a reference value of $|\mathbf{d}_{ee}| = 250\,\text{D} \approx e \times 5\,\text{nm}$, close to the values of a few $e \times$ nm that have been reported in nitride-based quantum dots [36,37]. It is also consistent with the electron-hole separation achieved in colloidal semiconductor quantum dot molecules [38], and below the large permanent dipole moment achieved in self-assembled quantum dot molecules, which can reach electron-hole separations of tens of nm [39,40]. Large permanent dipole moments offer an added benefit to source performance by exhibiting longer radiative lifetimes due to the reduced overlap between electron and hole wavefunctions [41].

This value of $|\mathbf{d}_{ee}|$ leads to coupling rates to the cavity modes L_1 and L_3 in the GHz range (see Table I). We set the Rabi frequency to $\Omega/2\pi = 0.2$ THz, in line with previous experimental reports with semiconductor quantum dots [42,43]. This choice requires different detunings $|\Delta|$ in each configuration to satisfy the resonance condition $\Omega_R = \omega_c$, yielding dressing ratios of $h = 0.0325$ for L_1 and $h = 0.019\,55$ for L_3. Finally, we set $\gamma/2\pi = 39.7\,\text{MHz}$, giving a lifetime of 4 ns typical for solid-state quantum emitters [35]. These parameters result in effective cooperativities $\tilde{C} = 1.94$ (for L_1) and $\tilde{C} = 24.65$ (for L_3), yielding a $P_{\max}$ of ∼60% and 90%, respectively.

Regarding sources of decoherence beyond spontaneous emission, we have shown (see Appendix I) that thermal noise and pure dephasing should have a negligible effect under standard helium cooling conditions.

Finally, the single-photon sensitivity required to directly verify our THz SPE in an HBT setup has been demonstrated in several classes of detectors, such as quantum dot SET detectors (∼0.5–3 THz) [44], charge-sensitive infrared phototransistors (∼6–30 THz) [45], and quantum-capacitance detectors (∼1.5 THz) [46].

VII. CONCLUSIONS

We have proposed an on-demand THz single-photon source featuring wide frequency tunability and optical heralding with efficiencies between 90% and 95% comparable to state-of-the-art nondeterministic parametric down-conversion sources [10,47–49]. Using our custom-designed hybrid THz cavities combined with optical quantum emitters with experimentally available permanent dipole moments, the scheme achieves high efficiencies (65%–92%) and purities (88%–100%) comparable to the best visible single-photon sources [35], requiring only standard helium cooling and optical lasers. The mechanism proposed enables heralding and complete characterization of photon statistics of the emitted THz state via detection of photons in the visible regime. Our source demonstrates the potential of optically dressed polar quantum emitters to enable the first experimental realizations of deterministic THz single-photon sources and to serve as a building block for developing quantum optics in this frequency regime.

ACKNOWLEDGMENTS

We acknowledge financial support from the Proyecto Sinérgico CAM 2020 Y2020/TCS-6545 (NanoQuCo-CM), and MCINN projects PID2021-126964OB-I00 (QENIGMA), TED2021-130552B-C21 (ADIQUNANO), PID2024-156077OB-I00 (DQUOTE), No. CEX2023-001316-M through the María de Maeztu program for Units of Excellence in RD and by the project NPhoQuss funded by Programa Fundamentos 2024 from the BBVA Foundation through the

Grant No. EIC24-1-17304. C.S.M. acknowledges support by Project No. PID2023-149969NA-100 (SEQUOIA) funded by the Spanish Agencia Estatal de Investigación MICIU/AEI/10.13039/501100011033, and by a 2025 Leonardo Grant for Scientific Research and Cultural Creation from the BBVA Foundation. C.S.M. and D.M.-C. also acknowledge support by the project NPhoQuss funded by Programa Fundamentos 2024 from the BBVA Foundation through the Grant No. EIC24-1-17304, and the support of a fellowship from la Caixa Foundation (ID 100010434), from the European Union's Horizon 2020 Research and Innovation Programme under the Marie Sklodowska-Curie Grant Agreement No. 847648, with fellowship codes LCF/BQ/PI20/11760026 and LCF/BQ/PI20/11760018. D.M.-C. also acknowledges support from the Ramon y Cajal program (RYC2020-029730-I). C.G. acknowledges support from the Knut and Alice Wallenberg Foundation through the Wallenberg Centre for Quantum Technology (WACQT). All authors thank Antonio I. Fernández-Domínguez for fruitful discussions and initial simulation support in the project.

DATA AVAILABILITY

The data that support the findings of this article are not publicly available. The data are available from the authors upon reasonable request.

APPENDIX A: INDISTINGUISHABILITY AND PURITY

One measure of the quality of a single-photon source is the indistinguishability of the emitted photons. The indistinguishability can be verified by a Hong-Ou-Mandel setup, where two subsequent one-photon pulses from the source are made to interfere on a beam splitter. The cross-correlations of the two output channels are [50]

$$G_{\mathrm{HOM}}(t,t') = \tfrac{1}{2}\big(G^{(2)}_{\mathrm{pop}}(t,t') + G^{(2)}(t,t') - |G^{(1)}(t,t')|^2\big), \tag{A1}$$

where the first- and second-order correlation functions employed are defined as

$$G^{(2)}_{\mathrm{pop}}(t,t') \equiv \langle \hat{a}^\dagger \hat{a}\rangle(t+t')\langle \hat{a}^\dagger \hat{a}\rangle(t), \tag{A2}$$

$$G^{(1)}(t,t') \equiv \langle \hat{a}^\dagger(t)\hat{a}(t+t')\rangle, \tag{A3}$$

$$G^{(2)}(t,t') \equiv \langle \hat{a}^\dagger(t)\hat{a}^\dagger(t+t')\hat{a}(t+t')\hat{a}(t)\rangle. \tag{A4}$$

The indistinguishability (or two-photon interference visibility) can then be computed by taking the ratio of the interference peaks at $t'=0$ and $t'=2\tau$ of a pulsed source with period 2τ [50]:

$$\begin{aligned} I &= 1 - \frac{\int_0^\tau dt \int_{-\tau}^{\tau} dt' G^{(2)}_{\mathrm{HOM}}(t,t')}{\int_0^\tau dt \int_{\tau}^{3\tau} dt' G^{(2)}_{\mathrm{HOM}}(t,t')} \\ &= 1 - \frac{\int_0^\tau dt \int_0^\tau dt' \big(G^{(2)}_{\mathrm{pop}}(t,t') + G^{(2)}(t,t') - |G^{(1)}(t,t')|^2\big)}{\int_0^\tau dt \int_0^\tau dt' \big(2G^{(2)}_{\mathrm{pop}}(t,t') - |\langle \hat{a}^\dagger(t)\rangle\langle \hat{a}(t+t')\rangle|^2\big)}. \end{aligned} \tag{A5}$$

This definition is the one adopted in the results for I shown in this text, which we compute via the quantum regression theorem. To obtain the purity, we compute the second-order degree of coherence over the pulse by dividing the two-photon probability by the squared integrated photon probability (both integrated over the pulse time), i.e.,

$$g^{(2)}(0) = \frac{\int_0^\tau dt \int_0^\tau dt' G^{(2)}(t,t')}{\int_0^\tau dt \int_0^\tau dt' G^{(2)}_{\mathrm{pop}}(t,t')}. \tag{A6}$$

In a regime where we are close to single-photon generation, the classical coherent amplitude should vanish, i.e., $|\langle \hat{a}^\dagger(t)\rangle\langle \hat{a}(t+t')\rangle|^2 \approx 0$. Using our adiabatic model $\mathcal{L}_{\mathrm{adb}}$, we can evaluate the correlation functions to be

$$\begin{aligned} G^{(2)}_{\mathrm{pop}}(t,t') &\sim \langle \hat{\xi}_+\hat{\xi}_-\rangle(t+t')\langle \hat{\xi}_+\hat{\xi}_-\rangle(t) \\ &= \begin{cases} \frac{(1+\tilde{C}e^{-\gamma(1+\tilde{C})t})(1+\tilde{C}e^{-\gamma(1+\tilde{C})(t+t')})}{(1+\tilde{C})^2}, & \Delta > 0, \\ e^{-\gamma(1+\tilde{C})(2t+t')}, & \Delta < 0, \end{cases} \end{aligned} \tag{A7}$$

$$\begin{aligned} G^{(1)}(t,t') &\sim \langle \hat{\xi}_+(t)\hat{\xi}_-(t+t')\rangle \\ &= \begin{cases} \frac{e^{-\gamma(1+\tilde{C})t'/2}(1+\tilde{C}e^{-\gamma(1+\tilde{C})t})}{1+\tilde{C}}, & \Delta > 0, \\ e^{-\gamma(1+\tilde{C})(2t+t')/2}, & \Delta < 0, \end{cases} \end{aligned} \tag{A8}$$

$$\begin{aligned} G^{(2)}(t,t') &\sim \langle \hat{\xi}_+(t)\hat{\xi}_+(t+t')\hat{\xi}_-(t+t')\hat{\xi}_-(t)\rangle \\ &= \begin{cases} \frac{(1-e^{-\gamma(1+\tilde{C})t'})(1+\tilde{C}e^{-\gamma(1+\tilde{C})t})}{(1+\tilde{C})^2}, & \Delta > 0, \\ 0, & \Delta < 0. \end{cases} \end{aligned} \tag{A9}$$

From this, one can see that $G^{(2)}(t,t') \approx G^{(2)}_{\mathrm{pop}}(t,t') - |G^{(1)}(t,t')|^2$, which leads to the purity following the indistinguishability.

APPENDIX B: ANALYTICAL EXPRESSIONS FOR THE MAXIMUM OF THE SINGLE-PHOTON PROBABILITY

1. Blue detuning $\Delta > 0$

We can derive an explicit expression for $P_1(\tau)$ using the simplified model given by $\mathcal{L}_{\mathrm{adb}}$ ($\mathcal{K}_{\mathrm{adb}} = \Gamma\hat{\xi}_-\hat{\rho}\hat{\xi}_+$), i.e.,

$$\begin{aligned} P_1(\tau) &= \int_0^\tau \mathrm{Tr}[e^{(\mathcal{L}_{\mathrm{adb}}-\mathcal{K}_{\mathrm{adb}})(\tau-t)}\mathcal{K}_{\mathrm{adb}}e^{(\mathcal{L}_{\mathrm{adb}}-\mathcal{K}_{\mathrm{adb}})t}\hat{\rho}_0]dt \\ &= \int_0^\tau \mathrm{Tr}\left[e^{(\mathcal{L}_{\mathrm{adb}}-\mathcal{K}_{\mathrm{adb}})(\tau-t)}\mathcal{K}_{\mathrm{adb}}\begin{pmatrix} e^{-\gamma\tilde{C}t} & 0 \\ 0 & 0 \end{pmatrix}\right]dt \\ &= \int_0^\tau \mathrm{Tr}\left[e^{(\mathcal{L}_{\mathrm{adb}}-\mathcal{K}_{\mathrm{adb}})(\tau-t)}\begin{pmatrix} 0 & 0 \\ 0 & \gamma\tilde{C}e^{-\gamma\tilde{C}t} \end{pmatrix}\right]dt \\ &= \int_0^\tau \mathrm{Tr}\begin{pmatrix} -\frac{\gamma^2\tilde{C}e^{-t\gamma\tilde{C}}(e^{-(\tau-t)\gamma}-e^{-(\tau-t)\gamma\tilde{C}})}{\gamma-\gamma\tilde{C}} & 0 \\ 0 & \gamma\tilde{C}e^{-t\gamma\tilde{C}}e^{-(\tau-t)\gamma} \end{pmatrix}dt \\ &= \frac{e^{-\tau\gamma} - e^{-\tau\gamma\tilde{C}}\big[1+\gamma\tau\big(1-\frac{1}{\tilde{C}}\big)\big]}{\big(1-\frac{1}{\tilde{C}}\big)^2}. \end{aligned} \tag{B1}$$

The exact solutions to the time and amplitude of the maximum of the single-photon emission probability in Eq. (1) are obtained by rewriting the condition $dP_1(\tau)/d\tau = 0$ as

$$\gamma\tau_{\max} = -1 - \frac{1}{\tilde{C}(\tilde{C}-1)} + \frac{1}{\tilde{C}-1}e^{\gamma\tau_{\max}(\tilde{C}-1)}, \tag{B2}$$

which is of the form $x = \alpha + \beta e^{\delta x}$ and has the general solution $x = \alpha - W(-\beta\delta e^{\alpha\delta})/\delta$, where W is the product logarithm (Lambert W function) [51]. This yields

$$\tau_{\max} = \frac{\gamma^{-1}}{1-\tilde{C}}\left(W_{-\theta(\tilde{C})}(\Xi) + \frac{1}{\tilde{C}} + \tilde{C} - 1\right) \tag{B3}$$

and

$$P_1(\tau_{\max}) = \exp\left[\frac{\frac{1}{\tilde{C}} + W_{-\theta(\tilde{C})}(\Xi)}{\tilde{C}-1}\right]\frac{\tilde{C} + W^{-1}_{-\theta(\tilde{C})}(\Xi)}{e^{-1}(\tilde{C}-1)}, \tag{B4}$$

where $\Xi = -e^{1-\tilde{C}-\frac{1}{\tilde{C}}}$ and $\theta(x)$ is the Heaviside step function. $W_0(x)$ and $W_{-1}(x)$ are the two real branches of the product logarithm. Evaluating $W_r(\Xi)$ for large or small values $\tilde{C}$ can be problematic, since in the limiting case $\Xi \to 0$ the functions $W_{-1}(0)$ and $1/W_0(0)$ are not defined. In the following, we present some useful approximations that can be used in these limits.

2. Limit $\tilde{C} \gg 1$

For large values of $\tilde{C}$, we can use the following upper bound as an approximation $W_{-1}(x) \leqslant \ln(-x) - \ln[-\ln(-x)]$ [51]. This yields a simplified expression $\gamma\tau_{\max} \approx \ln\tilde{C}/\tilde{C}$, which we can rewrite as

$$\tau_{\max} \approx \Gamma^{-1}\ln\tilde{C} \tag{B5}$$

and similarly for the maximum single-photon probability,

$$P_1(\tau_{\max}) \approx 1 - \frac{\ln\tilde{C}}{\tilde{C}}. \tag{B6}$$

3. Limit $\tilde{C} \ll 1$

For small values of $\tilde{C}$, we use a first-order Taylor expansion around 0, $W_0(x) = x + \mathcal{O}(x^2)$ [51]. This yields

$$\tau_{\max} \approx \Gamma^{-1} \tag{B7}$$

and

$$P_1(\tau_{\max}) \approx e^{-1}, \tag{B8}$$

where we used that $-\Xi \ll 1/\tilde{C}$.

4. Limit $\tilde{C} = 1$

Although $\tau_{\max}$, P_1, and $P_1(\tau_{\max})$ are undefined in $\tilde{C} = 1$, the limits are well defined, yielding

$$\lim_{\tilde{C}\to 1} P_1(\tau) = \gamma\tau(1 + \gamma\tau/2)e^{-\tau\gamma}, \tag{B9}$$

$$\lim_{\tilde{C}\to 1} \tau_{\max} = \sqrt{2}/\gamma, \tag{B10}$$

$$\lim_{\tilde{C}\to 1} P_1(\tau_{\max}) = (1+\sqrt{2})e^{-\sqrt{2}}. \tag{B11}$$

5. Limit $\gamma \gg \kappa, g$

The analytics in this limit remain mostly the same except that the roles of κ and γ are switched, as can be seen by adiabatically eliminating the emitter, i.e., $\mathcal{L}_{\text{adb}}\hat{\rho} = \frac{\kappa}{2}\mathcal{D}(\hat{a})\hat{\rho} + \frac{2g^2}{\gamma}\mathcal{D}(\hat{a}^\dagger)\hat{\rho}$. This yields

$$P(\tau) = \frac{e^{-\tau\kappa} - e^{-\tau\kappa\tilde{C}}\left[1 + \kappa\tau\left(1 - \frac{1}{\tilde{C}}\right)\right]}{\left(1 - \frac{1}{\tilde{C}}\right)^2}, \tag{B12}$$

$$P_0(\tau) = \exp(-\kappa\tilde{C}\tau), \tag{B13}$$

$$\kappa\tau_{\max} = -1 - \frac{1}{\tilde{C}(\tilde{C}-1)} - \frac{W_{-\theta(\tilde{C})}(\Xi)}{\tilde{C}-1}. \tag{B14}$$

6. Red detuning $\Delta < 0$

We can compute the zero-photon probability as before

$$P_0(\tau) = \int_0^\tau \mathrm{Tr}(S_\tau\hat{\rho}_0)dt = \frac{1}{\tilde{C}+1}(1 + \tilde{C}e^{-\tau(\gamma+\Gamma)}), \tag{B15}$$

from which we can obtain the complementary single-photon probability since the lack of the previously present incoherent pumping process removes the chance of repopulating the $|+\rangle\langle+|$ state and emission of a second THz photon

$$P_1(\tau) = 1 - P_0(\tau) = \frac{\tilde{C}}{\tilde{C}+1}[1 - e^{-\tau(\gamma+\Gamma)}]. \tag{B16}$$

P_1 is maximized for large times τ, i.e., there is no longer a timing issue. The maximal value is given by

$$P_{\max} = \frac{\tilde{C}}{\tilde{C}+1}. \tag{B17}$$

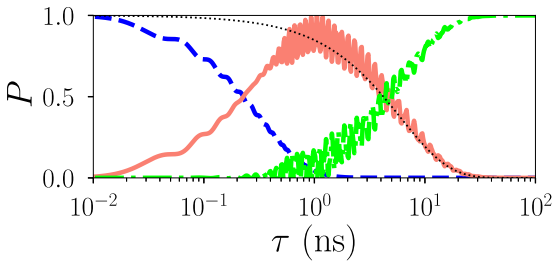


FIG. 4. Single-photon probability for a near-resonant drive $\Omega \sim \Omega_R$. The numerically computed single-photon probability $P_1(\tau)$ (solid red) is shown alongside the analytical prediction (dotted black) and the numerical probabilities of detecting zero photons $P_0(\tau)$ (dashed blue) and more than one photon $P_{>1}(\tau)$ (dash-dotted green), for the parameter set $\chi/2\pi = 12.5$ GHz, $\kappa/2\pi = 0.974$ GHz, $\gamma/2\pi = 39.78$ MHz, $\Omega/2\pi = 4$ THz, $\Delta/2\pi = 3.19$ THz, and $\omega_c/2\pi = 5.116$ THz.

APPENDIX C: THE NEAR-RESONANT REGIME

The near-resonant regime yields larger coupling strengths, which may suggest larger single-photon probabilities and shorter emission timescales. However, the subsequent change in the dressing ratio compromises the assumption that $\gamma_\pm$ can be neglected, and the effective cooperativity becomes more accurately described [20] by

$$\tilde{C} = \frac{4g^2}{\kappa(\gamma_- + \gamma_+)} = \frac{4C}{h^2 + h^{-2}}. \tag{C1}$$

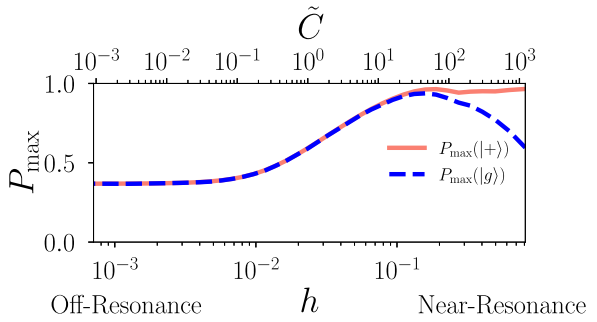


FIG. 5. Single-photon probability for different initial states. Maximum single-photon detection probability $P_{\max}$, obtained numerically (solid red) as a function of the detuning Δ for the parameter set $\{\chi, \kappa, \gamma, \Omega, \Omega_R\}/2\pi = \{4, 3.5, 39.78, 0.2, 3078\}$ GHz. The dashed blue line in the bottom plot represents the situation where the initial state is $|g\rangle$.

Assuming that the adiabatic elimination still holds, the general single-photon probability is given by

$$P_1(\tau) = \frac{-2g^2}{A}\frac{e^{-\tau\left(\gamma_- + \gamma_+ + \frac{4g^2}{\kappa}\right)}[f(A) - f(-A)]}{[4g^2 + (\gamma_- + \gamma_+)\kappa]^2 - 16g^2\gamma_+\kappa}, \tag{C2}$$

where

$$A \equiv \sqrt{16g^4 + 8g^2(\gamma_- - \gamma_+)\kappa + (\gamma_- + \gamma_+)^2\kappa^2} \tag{C3}$$

and

$$\begin{aligned} f(A) \equiv\, & e^{\frac{\tau}{2\kappa}(4g^2+\gamma_-\kappa+\gamma_+\kappa-A)} \\ & \times [\kappa(\gamma_- + \gamma_+)[\gamma_+\tau(\kappa(\gamma_- + \gamma_+) - A) + 2\gamma_-\kappa] \\ & + 4g^2[\gamma_+\tau(A + 2\gamma_-\kappa - 2\gamma_+\kappa) + 4\gamma_-\kappa - 2\gamma_+\kappa] \\ & + 16g^4(\gamma_+\tau + 2)]. \end{aligned} \tag{C4}$$

In the resonant limit, we have $\gamma_- \approx \gamma_+ \approx \gamma/4$ and $g \approx \chi$ ($\tilde{C} = 2C$), which we can use to simplify further the expression of the single-photon probability,

$$\begin{aligned} P_1(\tau) = \frac{e^{-\gamma\tau\left(1+\frac{C}{2}+\sqrt{1+4C^2}\right)}}{(1+4C^2)^{\frac{3}{2}}}\Bigg\{ & C^3(-1 + e^{\gamma\tau\sqrt{1+4C^2}})(8 + \gamma\tau) - \frac{C^2}{2}[4(-1 + e^{\gamma\tau\sqrt{1+4C^2}}) \\ & - (1 + e^{\gamma\tau\sqrt{1+4C^2}})\gamma\tau\sqrt{1+4C^2}] + \frac{C}{4}[(-1 + e^{\gamma\tau\sqrt{1+4C^2}})(4 + \gamma\tau) + (1 + e^{\gamma\tau\sqrt{1+4C^2}})\gamma\tau\sqrt{1+4C^2}]\Bigg\}. \end{aligned} \tag{C5}$$

Figure 4 shows numeric and analytic results for the single-photon probability close to resonance. Since g/κ ratio is larger than in the regime of parameters considered in the main text, the analytical results are worse at capturing the fast transient rise, failing to capture the oscillations of P_1 in time due to vacuum Rabi oscillations of the THz photon. Nevertheless, Eq. (C2) still matches the average P_1 pretty well in the long-time limit. The oscillations introduce fluctuations in the optimal pulse length $\tau_{\max}$, accounting for its nonmonotonic behavior near resonance in Fig. 3.

APPENDIX D: THE OFF-RESONANT REGIME

For $\Delta > 0$, operating in the off-resonant regime offers several advantages that may compensate for the reduction in effective coupling strength. One clear benefit is that achieving generalized Rabi frequencies Ω_R well within the THz range becomes feasible with lower driving amplitudes Ω, and therefore reduced optical power. Another advantage is that the required initial state becomes close to the ground state of the bare qubit, since for $\Delta \gg \Omega$, we find $|\langle g|+\rangle| = c \approx 1$. This means that, for a detuning Δ large enough, one could simplify the experimental protocol by omitting the first preparation pulse that initializes the state $|+\rangle$. Figure 5 shows the performance of the scheme when dispensing the preparation pulse and when using $|g\rangle$ as the initial state. A deviation from the results obtained with the optimal initial state $|+\rangle$ is only noticeable for $h > 10^{-1}$, i.e., $1 - \Delta/\Omega_R > 10^{-2}$, which corresponds to $c \approx 1 + (\Delta/\Omega_R - 1)/4 \lesssim 0.998$. Assuming that we can achieve a C large enough that $\tilde{C} \gg 10$, we can solve $P_{\max} = 1 - \ln\tilde{C}/\tilde{C}$ for $\tilde{C}$ and obtain

$$\tilde{C} = \exp[-W_{-1}(P_{\max} - 1)]. \tag{D1}$$

Using this equation and that outside of the near-resonant regime, we can approximate $\tilde{C} \approx 4s^2C \approx C\Omega^2/\Omega_R^2 \approx C\Omega^2/\Delta^2$, we can find the bounds for, e.g., C or Δ that could achieve a certain $P_{\max}$ depending on what we assume to be fixed.

APPENDIX E: EFFICIENCY VERSUS PURITY

For $\Delta > 0$, whether the main limitation for perfect single-photon generation is efficiency or purity depends on the effective cooperativity $\tilde{C}$. Figure 6 shows the dependence of the probabilities of measuring zero $[P_0(\tau_{\max})]$, one $[P_{\max} = P_1(\tau_{\max})]$, or more than one $[P_{>1}(\tau_{\max})]$ photons at the optimal pulse length $\tau_{\max}$ as a function of the effective cooperativity $\tilde{C}$.

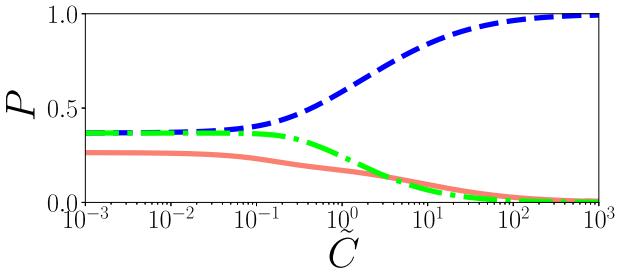


FIG. 6. Plot of the maximum single-photon detection probability $P_1(\tau_{\max})$ (dashed blue), $P_0(\tau_{\max})$ (dash-dotted green), and $P_{>1}(\tau_{\max})$ (solid red) as a function of $\tilde{C}$.

We find that $P_{>1}(\tau_{\max}) > P_0(\tau_{\max})$ in the limit of large $\tilde{C}$, while the opposite is true for small $\tilde{C}$. In the relevant limit of large $\tilde{C}$, where $P_{\max} \to 1 - \ln\tilde{C}/\tilde{C}$, the vacuum and multiphoton sources of imperfection are given by

$$P_0(\tau_{\max}) = \frac{1}{\tilde{C}}, \quad P_{>1}(\tau_{\max}) = \frac{\ln\tilde{C} - 1}{\tilde{C}}. \tag{E1}$$

Assuming that at $\tau_{\max}$ the two-photon probability $P_2(\tau_{\max})$ is roughly equal to $P_{>1}(\tau_{\max})$, and that detecting one photon is by far the most likely outcome $P \gg P_0(\tau_{\max}), P_{>1}(\tau_{\max})$, the single-photon purity can be estimated as

$$\Pi(\tau_{\max}) = 1 - g^{(2)}(0) \approx 1 - 2\frac{\ln\tilde{C}}{\tilde{C}}. \tag{E2}$$

In the limit of low $\tilde{C}$, we find $P_{>1} \to 1 - 2e^{-1}$.

APPENDIX F: REALISTIC LASER PULSE SHAPES

We assume throughout this work that the various pulses are turned on and off instantaneously, which is a justified approximation since the typical rise and fall times are on the order of hundreds of picoseconds and hundreds of femtoseconds [52,53], respectively. This time is much shorter than the expected decay in our setups, which are on the order of nanoseconds or more. Nevertheless, given that experimental laser pulses do not exhibit the idealized square form assumed in this work, in this section we investigate the influence of a more realistic time-dependent pulse that features a finite rise and fall time given by τ_p, and that is turned off at a time τ:

$$\Omega(t) = \begin{cases} 1 - e^{-\frac{t}{\tau_p}}, & t < \tau, \\ e^{-\frac{t}{\tau_p}}, & t > \tau. \end{cases} \tag{F1}$$

Importantly, this time dependence affects the dynamical composition of the dressed states $|\pm\rangle$, the coupling g, and the spontaneous processes $\gamma_{\pm,z}$. We base our simulations on quantum trajectories of the effective Jaynes-Cummings model with $\hat{H}_{\rm JC}$.

Figure 7(a) shows that a finite rise time delays the onset of $P_1(\tau)$ for $\tau < \tau_{\max}$, compared to the analytical results assuming an instantaneous rise. In addition, Fig. 7(b) shows the map $P_1(\tau)$ as a function of the pulse length and the rise time. We conclude from this map that the timescale of the rise time of the laser pulse has no noticeable influence on the dynamics of the single-photon probability as long as $\tau_{\max} > \tau_p$. However, once both timescales are comparable, we observe a temporal shift of the maximum P_1 to larger times. The dynamics at large τ are not affected, as the decay rates are typically much lower than the inverse fall time $\gamma, \Gamma \ll \tau_p^{-1}$. Typical rise times are on the order of hundreds of picoseconds, while typical fall times are on the order of hundreds of femtoseconds [52,53]. Since the expected decay time in realistic setups will be on the order of at least nanoseconds, we conclude that considering the laser ramp as effectively instantaneous is justified.

APPENDIX G: HERALDING

While spontaneous emission at optical frequencies tends to degrade single-photon emission due to repumping of the quantum emitter and subsequent multiphoton contributions, it also provides a potential pathway for optical heralding of THz photon emission, as discussed in detail in this Appendix and summarized in Fig. 8.

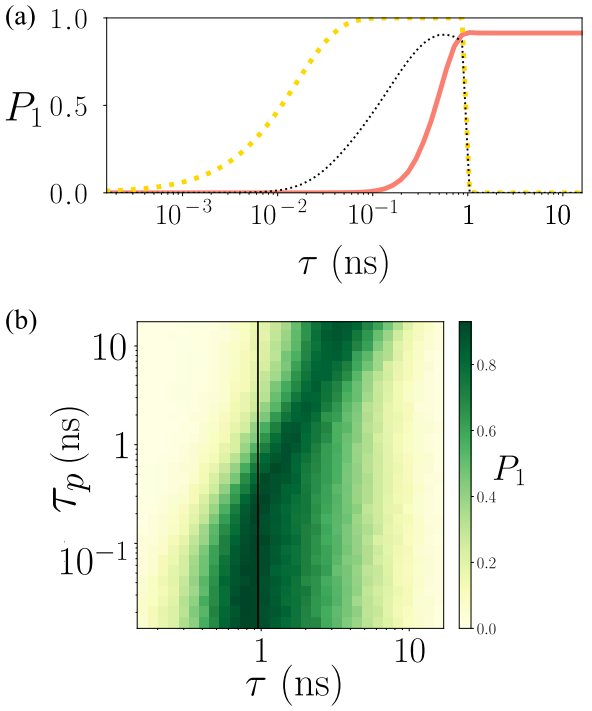


FIG. 7. Single-photon probability for nonsquare pulses. (a) $P_1(\tau)$ obtained numerically from 10^4 quantum trajectories (solid red) and analytically (dotted black), and the temporal profile of the laser drive (dotted yellow) for the parameter set $\{\chi, \kappa, \gamma, \Omega, \Omega_R, \tau_p^{-1}\}/2\pi = \{12.5, 0.974, 39.79 \times 10^{-3}, 0.2, 5116, 10^{-2}\}$ GHz. The shut-off is not instantaneous (even though it might appear so in the plot due to the logarithmic scale). (b) Map of the Maximum single-photon detection probability obtained numerically from 1000 quantum trajectories, as a function of the pulse length τ and the raising time τ_p for the parameter set $\{\chi, \kappa, \gamma, \Omega, \Omega_R\}/2\pi = \{12.5, 0.974, 39.79 \times 10^{-3}, 0.2, 5116\}$ GHz. The black line represents $\tau_{\max}$ for instantaneous rise and fall times.

In every individual realization of the experiment (a single trajectory in the quantum trajectory picture), a system that has not undergone optical spontaneous emission (no optical photodetection) is in one of these two possible states:

(1) Before THz-photon emission from the THz cavity:

$$|\psi_1\rangle = \alpha|+\rangle|0\rangle_{\rm THz} + \beta|-\rangle|1\rangle_{\rm THz}, \quad (\alpha \gg \beta)$$

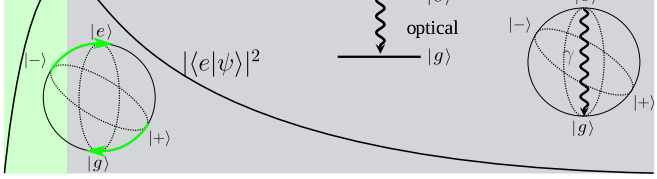


FIG. 8. Sketch of the temporal evolution of the population of $|e\rangle$ during the heralding sequence, including Bloch sphere representation.

(2) After THz-photon emission from the THz cavity:

$$|\psi_2\rangle = |-\rangle|0\rangle_{\mathrm{THz}}.$$

We recall that the emission of a THz photon is given by the collapse superoperator

$$\mathcal{K}\hat{\rho} \equiv \kappa \hat{X}\hat{\rho}\hat{X}^{\dagger}. \tag{G1}$$

On the other hand, spontaneous emission of an optical photon is described by the superoperator

$$\mathcal{K}_{\mathrm{opt}}\hat{\rho} \equiv \gamma \hat{\sigma}_{-}\hat{\rho}\hat{\sigma}_{+}, \tag{G2}$$

which is the only way the system can go from $|-\rangle$ to $|+\rangle$, thus restarting the cycle and allowing to generate more THz photons. Therefore, checking that no optical photon is emitted before turning off the laser at a time τ guarantees the emission of at most one single THz photon.

In order to determine whether a THz photon has been emitted in the first place, we can apply a second pulse after turning off the laser at time τ. The pulse must implement the unitary transformation

$$\hat{U} = \exp(-i\theta\hat{\sigma}_y), \tag{G3}$$

which transforms the emitter as $|\pm\rangle \to |g/e\rangle$, and therefore the states as

$$|\psi_1\rangle \to \alpha|g,0\rangle_{\mathrm{THz}} + \beta|e,1\rangle_{\mathrm{THz}}, \tag{G4}$$

$$|\psi_2\rangle \to |e,0\rangle_{\mathrm{THz}}. \tag{G5}$$

We can write the action of this pulse in superoperator form as

$$\mathcal{U} \equiv \hat{U}\hat{\rho}\hat{U}^{\dagger}. \tag{G6}$$

After this pulse, we let the system evolve freely described under the Liouvillian $\mathcal{L}_0\hat{\rho} = \frac{\kappa}{2}\mathcal{D}[\hat{a}]\hat{\rho} + \frac{\gamma}{2}\mathcal{D}[\hat{\sigma}_-]\hat{\rho}$ for a time long enough to observe all potential decays, e.g., $\tau' = 30/\gamma$. It is straightforward to see that the emission of an optical photon due to the relaxation from the excited state $|e\rangle$ is only compatible with states in which a THz photon was put into the cavity (which is eventually emitted), thus heralding the emission of the THz photon.

Based on this intuition, we can define two heralding protocols. The first protocol relies solely on the detection of a second optical photon after the activation pulse. While a THz photon can also exit the cavity at times $t > \tau$, the probability of this event is small under the assumption of a strongly dissipative THz cavity, so we rule it out of our calculations for the sake of simplicity. This allows us to write the efficiency of this protocol as

$$\begin{aligned} E &= P(\mathrm{THz}_{<\tau}|\mathrm{optical}_{>\tau}) = \frac{P(\mathrm{THz}_{<\tau}\cap \mathrm{optical}_{>\tau})}{P(\mathrm{optical}_{>\tau})} \\ &= \frac{\int_0^{\tau'} dt' \int_0^{\tau} dt\, \mathrm{Tr}[e^{(\mathcal{L}_0-\mathcal{K}_{\mathrm{opt}})(\tau'-t')}\,\mathcal{K}_{\mathrm{opt}}\, e^{(\mathcal{L}_0-\mathcal{K}_{\mathrm{opt}})t'}\mathcal{U}\, e^{(\mathcal{L}-\mathcal{K})(\tau-t)}\,\mathcal{K}\, e^{(\mathcal{L}-\mathcal{K})t}\hat{\rho}_0]}{\int_0^{\tau'} dt'\, \mathrm{Tr}[e^{(\mathcal{L}_0-\mathcal{K}_{\mathrm{opt}})(\tau'-t')}\,\mathcal{K}_{\mathrm{opt}}\, e^{(\mathcal{L}_0-\mathcal{K}_{\mathrm{opt}})t'}\mathcal{U}\, e^{\mathcal{L}\tau}\hat{\rho}_0]}, \end{aligned} \tag{G7}$$

where $\mathrm{THz}_{<\tau}$ refers to the emission of a single THz photon during the activation pulse of duration τ and $\mathrm{optical}_{>\tau}$ to the emission of a single optical photon after the activation and $\hat{U}$ pulses.

The second protocol, in contrast, heralds the THz photon based on two conditions: The absence of detection of the first optical photon at times $t < \tau$ before the activation pulse is turned off, and the detection of a single optical photon at a later time $t > \tau$. The associated heralding efficiency (conditional probability) [54,55] of this protocol is given by

$$\begin{aligned} \tilde{E} &= P(\mathrm{THz}_{<\tau}|\mathrm{no\ optical}_{<\tau}\cap \mathrm{optical}_{>\tau}) = \frac{P(\mathrm{THz}_{<\tau}\cap \mathrm{no\ optical}_{<\tau}\cap \mathrm{optical}_{>\tau})}{P(\mathrm{no\ optical}_{<\tau}\cap \mathrm{optical}_{>\tau})} \\ &= \frac{\int_0^{\tau'} dt' \int_0^{\tau} dt\, \mathrm{Tr}\big[e^{(\mathcal{L}_0-\mathcal{K}_{\mathrm{opt}})(\tau'-t')}\,\mathcal{K}_{\mathrm{opt}}\, e^{(\mathcal{L}_0-\mathcal{K}_{\mathrm{opt}})t'}\mathcal{U}\, e^{(\mathcal{L}-\mathcal{K}-\mathcal{K}_{\mathrm{opt}})(\tau-t)}\,\mathcal{K}\, e^{(\mathcal{L}-\mathcal{K}-\mathcal{K}_{\mathrm{opt}})t}\hat{\rho}_0\big]}{\int_0^{\tau'} dt'\, \mathrm{Tr}\big[e^{(\mathcal{L}_0-\mathcal{K}_{\mathrm{opt}})(\tau'-t')}\,\mathcal{K}_{\mathrm{opt}}\, e^{(\mathcal{L}_0-\mathcal{K}_{\mathrm{opt}})t'}\mathcal{U}\, e^{(\mathcal{L}-\mathcal{K}_{\mathrm{opt}})\tau}\hat{\rho}_0\big]}. \end{aligned} \tag{G8}$$

$\tilde{E}$ corresponds to the ideal heralding protocol, but it is much more challenging to implement, since measuring "no early optical" requires extremely high detection efficiencies. In contrast, E is an alternative easier to implement, which, however, does not rule out multiphoton emission of THz photons.

APPENDIX H: EFFICIENT COMPUTATION OF TIME INTEGRALS OF MULTITIME CORRELATORS VIA LIOUVILLIAN SPECTRAL DECOMPOSITION

In this Appendix, we outline efficient vectorized methods to compute the time integrals of multitime correlators—quantities that are central for many of the results presented in this paper—in terms of matrix multiplications involving only eigenvectors and eigenvalues of the Liouvillian.

1. Computing right and left eigenvector matrices

We define the ith right and left eigenvectors of the Liouvillian as

$$\mathcal{L}|r_i\rangle \equiv \mathcal{L}\mathbf{r}_i^T = \lambda_i \mathbf{r}_i^T, \tag{H1}$$

$$\langle l_i|\mathcal{L} \equiv \mathbf{l}_i\mathcal{L} = \lambda_i \mathbf{l}_i, \tag{H2}$$

where $\mathbf{r}_i$ and $\mathbf{l}_i$ are row vectors, i.e., $1 \times N$ matrices $\mathbf{r_i} = (r_{i,1}, r_{i,2}, \ldots, r_{i,N})$, $\mathbf{l_i} = (l_{i,1}, l_{i,2}, \ldots, l_{i,N})$, with $N = h^2$, where h is the dimension of the Hilbert space. Each of these objects is to be understood as $h \times h$ matrices arranged in vectorized form. In bra-ket notation, $|r_i\rangle$ is therefore represented as a column vector, ${\mathbf{r_i}}^T$. The whole set of eigenvectors can be efficiently represented as $N \times N$ eigenvector matrices

$$R \equiv \begin{pmatrix} \mathbf{r}_1 \\ \mathbf{r}_2 \\ \vdots \\ \mathbf{r}_N \end{pmatrix}, \qquad L \equiv \begin{pmatrix} \mathbf{l}_1 \\ \mathbf{l}_2 \\ \vdots \\ \mathbf{l}_N \end{pmatrix}, \tag{H3}$$

with the corresponding column vector, i.e., $N \times 1$ matrix of eigenvalues

$$\boldsymbol{\lambda} \equiv \begin{pmatrix} \lambda_1 \\ \lambda_2 \\ \vdots \\ \lambda_N \end{pmatrix}. \tag{H4}$$

The normalization condition $\mathbf{l}_i \cdot \mathbf{r}_j = \delta_{ij}$ can then simply be expressed as

$$L \cdot R^T = \mathbb{I}. \tag{H5}$$

In order to compute an orthogonalized set, a more robust method than solving the eigenvalue equations (H1) and (H2) independently and then normalizing is to first solve Eq. (H1) to obtain R. The matrix L of left eigenvectors can then be found by enforcing Eq. (H5), which amounts to computing the inverse of the matrix of right eigenvectors

$$L = (R^T)^{-1}. \tag{H6}$$

Working with the eigenvector matrices directly will give us a massive computational advantage, since it will allow us to use vectorized operations for the calculation of Liouvillian evolution. This efficiency becomes especially important when computing more complex quantities, such as integrals of multitime correlation operators, as we will demonstrate in the next sections. These derivations will make extensive use of the following spectral decomposition of Liouvillian evolution:

$$e^{\mathcal{L}t} = \sum_i e^{\lambda_i t} |r_i\rangle\langle l_i|. \tag{H7}$$

2. Calculation of single-photon probability $P(\tau)$

We are interested in evaluating time-integrated two-time correlation functions of the form

$$P(\tau) = \int_0^\tau \mathrm{Tr}[e^{\mathcal{L}(\tau-t)}\,\mathcal{K}\,e^{\mathcal{L}t}\rho_0]dt, \tag{H8}$$

where ρ_0 is the initial density matrix and $\mathcal{K}$ is a quantum jump superoperator (e.g., representing a photon detection event). We will now adopt the bra-ket notation, in which a density matrix ρ is represented as a ket $|\rho\rangle$. The representation of this object in algebraic (row vector) form will be denoted as $\boldsymbol{\rho}$. The trace operation can then generally be expressed as $\mathrm{Tr}[\rho] = \langle\mathbb{I}|\rho\rangle = \mathbf{1}\cdot\boldsymbol{\rho}^T$, where $|\mathbb{I}\rangle$ is the vectorized form of the identity matrix in bra-ket notation and $\mathbf{1}$ is its algebraic (row-vector) representation. Using the spectral decomposition of the Liouvillian, Eq. (H7), we can expand the integrand in Eq. (H8) as

$$\begin{aligned} P(\tau) &= \int_0^\tau \mathrm{Tr}\left[\sum_{i,j} e^{\lambda_j(\tau-t)}e^{\lambda_i t}|r_j\rangle\langle l_j|\,\mathcal{K}\,|r_i\rangle\langle l_i|\rho_0\rangle\right]dt \\ &= \sum_{i,j} \underbrace{\langle\mathbb{I}|r_j\rangle}_{\equiv T_j} \underbrace{\left(\int_0^\tau dt\, e^{\lambda_j(\tau-t)}e^{\lambda_i t}\right)\langle l_j|\mathcal{K}|r_i\rangle}_{\equiv A_{ji}} \underbrace{\langle l_i|\rho_0\rangle}_{\equiv C_i} \\ &= T\cdot A\cdot C^T, \end{aligned} \tag{H9}$$

where the terms of the sum have been grouped to represent elements of the $N \times N$ matrix A, and the N-dimensional vectors T and C, which we defined as

$$T_j \equiv \langle\mathbb{I}|r_j\rangle, \tag{H10}$$

$$A_{ji} \equiv \left(\int_0^\tau dt\, e^{\lambda_j(\tau-t)}e^{\lambda_i t}\right)\langle l_j|\mathcal{K}|r_i\rangle, \tag{H11}$$

$$C_i \equiv \langle l_i|\rho_0\rangle. \tag{H12}$$

We can further decompose the matrix A as the Hadamard (elementwise) product of two matrices, $A = I(\tau)\odot B$, where

$$I_{ji}(\tau;\boldsymbol{\lambda}) \equiv \int_0^\tau dt\, e^{\lambda_j(\tau-t)}e^{\lambda_i t} \tag{H13}$$

$$= \begin{cases} \tau e^{\lambda_i\tau}, & \text{if } \lambda_i = \lambda_j, \\ \frac{e^{\lambda_i\tau}-e^{\lambda_j\tau}}{\lambda_i-\lambda_j}, & \text{otherwise}, \end{cases} \tag{H14}$$

$$B_{ji} \equiv \langle l_j|\mathcal{K}|r_i\rangle. \tag{H15}$$

If we have previously computed the eigenvector matrices R and L, the efficiency of the calculation of $P(\tau)$ can be greatly enhanced by precomputing the vectors T, C, and the matrix B from Eqs. (H10), (H12), and (H15), respectively. Using directly the eigenvector matrices, these objects can be written in a compact and computationally convenient form based on matrix multiplications:

$$T = \mathbf{1}\cdot R^T, \tag{H16}$$

$$B = L\cdot\mathcal{K}\cdot R^T, \tag{H17}$$

$$C = L\cdot\boldsymbol{\rho}_0^T. \tag{H18}$$

Having precomputed these quantities, evaluating $P(\tau)$ at different values of τ only requires evaluating the $I(\tau)$ matrix according to Eq. (H14), and then performing the matrix multiplication:

$$P(\tau) = T\cdot(B\odot I(\tau))\cdot C. \tag{H19}$$

3. Calculation of heralding efficiencies

The method outlined above can be extended to compute more complex quantities, such as the heralding efficiencies $E(\tau',\tau)$ and $\tilde{E}(\tau',\tau)$, introduced in the previous section. Before reminding the explicit expressions of E and $\tilde{E}$, let us define some relevant effective Liouvillian operators that will

be used in their definition, as well as its eigenvectors:

$$\begin{aligned} &S \equiv \mathcal{L} - \mathcal{K} - \mathcal{K}_{\rm opt}, && \text{with } S|r_i\rangle = \lambda_i|r_i\rangle, \\ &S' \equiv \mathcal{L}_0 - \mathcal{K}_{\rm opt}, && \text{with } S'|r_i'\rangle = \lambda_i'|r_i'\rangle, \\ &S'' \equiv \mathcal{L} - \mathcal{K}_{\rm opt}, && \text{with } S''|r_i''\rangle = \lambda_i''|r_i''\rangle, \\ &S''' \equiv \mathcal{L} - \mathcal{K}, && \text{with } S'''|r_i'''\rangle = \lambda_i'''|r_i'''\rangle, \\ &S_0 \equiv \mathcal{L}, && \text{with } S_0|r_i^0\rangle = \lambda_i^0|r_i^0\rangle. \end{aligned} \tag{H20}$$

a. Heralding efficiency $\tilde{E}$

The heralding efficiency $\tilde{E}$ is then defined as the ratio between two time-integrated two-time correlation expressions, $\tilde{E} = \tilde{N}/\tilde{D}$, where

$$\tilde{N} = \int_0^{\tau'} dt' \int_0^{\tau} dt\, \mathrm{Tr}[e^{S'(\tau'-t')}\mathcal{K}_{\rm opt}e^{S't'}\mathcal{U} \times e^{S(\tau-t)}\,\mathcal{K}\,e^{St}\rho_0], \tag{H21}$$

$$\tilde{D} = \int_0^{\tau'} dt'\, \mathrm{Tr}[e^{S'(\tau'-t')}\,\mathcal{K}_{\rm opt}\,e^{S't'}\mathcal{U}e^{S''\tau}\rho_0]. \tag{H22}$$

To evaluate these expressions, we follow the same procedure as in the previous section. Using the spectral decomposition of these Liouvillians and the definition of the integrated exponentials of Eq. (H14), numerator and denominator become

$$\tilde{N} = \sum_{m,n,i,j} \underbrace{\langle \mathbb{I}|r_m'\rangle}_{\equiv T_m}\, I_{mn}(\tau',\boldsymbol{\lambda}')\, \underbrace{\langle l_m'|\mathcal{K}_{\rm opt}|r_n'\rangle}_{\equiv B'_{mn}}\, \underbrace{\langle l_n'|\mathcal{U}|r_j\rangle}_{\equiv Q_{nj}}\, I_{ji}(\tau,\boldsymbol{\lambda})\, \underbrace{\langle l_j|\mathcal{K}|r_i\rangle}_{B_{ji}}\, \underbrace{\langle l_i|\rho_0\rangle}_{Y_i}, \tag{H23}$$

$$\tilde{D} = \sum_{m,n,i} \underbrace{\langle \mathbb{I}|r_m'\rangle}_{\equiv T_m}\, I_{mn}(\tau',\boldsymbol{\lambda}')\, \underbrace{\langle l_m'|\mathcal{K}_{\rm opt}|r_n'\rangle}_{\equiv B'_{mn}}\, \underbrace{\langle l_n'|\mathcal{U}|r_i''\rangle}_{\equiv Q'_{ni}}\, e^{\lambda_i''\tau}\, \underbrace{\langle l_i''|\rho_0\rangle}_{Y_i''}, \tag{H24}$$

where each term is defined as

$$T_m \equiv \langle \mathbb{I}|r_m'\rangle, \tag{H25}$$

$$B'_{mn} \equiv \langle l_m'|\mathcal{K}_{\rm opt}|r_n'\rangle, \tag{H26}$$

$$B_{ji} \equiv \langle l_j|\mathcal{K}|r_i\rangle, \tag{H27}$$

$$Q_{nj} \equiv \langle l_n'|\mathcal{U}|r_j\rangle, \tag{H28}$$

$$Q'_{ni} \equiv \langle l_n'|\mathcal{U}|r_i''\rangle, \tag{H29}$$

$$Y_i \equiv \langle l_i|\rho_0\rangle, \tag{H30}$$

$$Y_i'' \equiv \langle l_i''|\rho_0\rangle. \tag{H31}$$

Now, we can write these matrices using the eigenvector matrices as in the previous section:

$$T = \mathbf{1}\cdot(R')^T, \tag{H32}$$

$$B' = L'\cdot\mathcal{K}_{\rm opt}\cdot(R')^T, \tag{H33}$$

$$B = L\cdot\mathcal{K}\cdot R^T, \tag{H34}$$

$$Q = L'\cdot\mathcal{U}\cdot R^T, \tag{H35}$$

$$Q' = L'\cdot\mathcal{U}\cdot(R'')^T, \tag{H36}$$

$$Y = L\cdot\boldsymbol{\rho}_0^T, \tag{H37}$$

$$Y'' = L''\cdot\boldsymbol{\rho}_0^T. \tag{H38}$$

Thus, the full expressions for the numerator and denominator take the following expressions in terms of matrix products, which benefit greatly from the precomputation of the matrices defined above:

$$\tilde{N} = T\cdot(I(\tau';\boldsymbol{\lambda}')\odot B')\cdot Q\cdot(I(\tau;\boldsymbol{\lambda})\odot B)\cdot Y, \tag{H39}$$

$$\tilde{D} = T\cdot(I(\tau';\boldsymbol{\lambda}')\odot B')\cdot Q'\cdot(e^{\boldsymbol{\lambda}''\tau}\odot Y''), \tag{H40}$$

where we used the notation $\boldsymbol{\lambda}$ to denote the vector of eigenvalues.

b. Heralding efficiency E

Similarly to the previous case, the heralding efficiency E is defined as a ratio $E = N/D$, where now

$$N = \int_0^{\tau'} dt' \int_0^{\tau} dt\, \mathrm{Tr}[e^{S'(\tau'-t')}\mathcal{K}_{\rm opt}e^{S't'}\mathcal{U}e^{S'''(\tau-t)}\,\mathcal{K}\,e^{S'''t}\rho_0], \tag{H41}$$

$$D = \int_0^{\tau'} dt'\, \mathrm{Tr}[e^{S'(\tau'-t')}\,\mathcal{K}_{\rm opt}\,e^{S't'}\mathcal{U}e^{S_0\tau}\rho_0]. \tag{H42}$$

The calculation is analogous as before. Defining in this case the slightly different matrices

$$T = \mathbf{1}\cdot(R')^T, \tag{H43}$$

$$B' = L'\cdot\mathcal{K}_{\rm opt}\cdot(R')^T, \tag{H44}$$

$$B = L'''\cdot\mathcal{K}\cdot(R''')^T, \tag{H45}$$

$$Q = L'\cdot\mathcal{U}\cdot(R''')^T, \tag{H46}$$

$$Q' = L'\cdot\mathcal{U}\cdot(R^0)^T, \tag{H47}$$

$$Y = L'''\cdot\boldsymbol{\rho}_0^T, \tag{H48}$$

$$Y'' = L^0\cdot\boldsymbol{\rho}_0^T, \tag{H49}$$

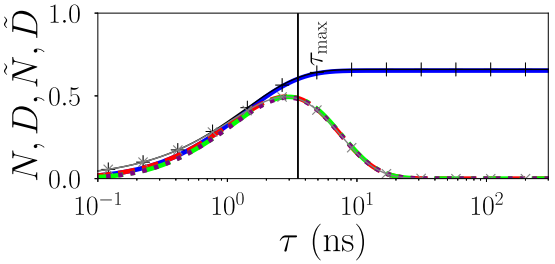


FIG. 9. The probabilities $\tilde{N}$ (dash-dotted purple), N (dashed green), $\tilde{D}$ (dashed red), D (solid blue), and the analytics for $\tilde{N}, N, \tilde{D}$ (gray ×'s), and D (black +'s) as a function of time for the parameter set $\{\gamma, \kappa, \chi, \Omega_R\}/2\pi = \{39.79 \times 10^{-3}, 3.5, 4, 3078\}$ GHz.

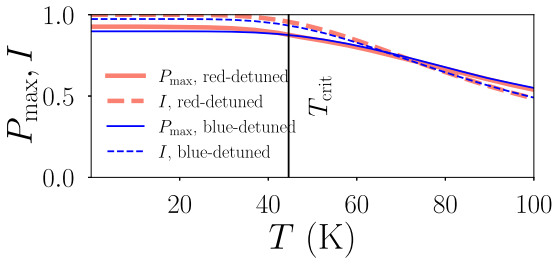


FIG. 10. Numerical results for maximum single-photon detection probability $P_{\max}$ (solid) and indistinguishability I (dashed) as a function of the temperature T for the parameter set $\{\chi, \kappa, \gamma, \Omega, \Omega_R\}/2\pi = \{12.5, 0.974, 39.78 \times 10^{-3}, 0.2, 5116\}$ GHz for $\Delta > 0$ (blue) and $\Delta < 0$ (red). The black vertical lines represent the critical value T_{crit}, where the thermal noise is estimated to begin to dominate.

the result is expressed as

$$N = T \cdot (I(\tau'; \boldsymbol{\lambda}') \odot B') \cdot Q \cdot (I(\tau; \boldsymbol{\lambda}''') \odot B) \cdot Y, \tag{H50}$$

$$D = T \cdot (I(\tau'; \boldsymbol{\lambda}') \odot B') \cdot Q' \cdot (e^{\boldsymbol{\lambda}^{\mathbf{0}}\tau} \odot Y''). \tag{H51}$$

c. Analytical expressions for the Heralding efficiency

Following the procedure in Eq. (B1), we can obtain analytical results for D and N. This requires that the model $\mathcal{L}_{\text{adb}}$ is valid ($\Delta \gg \Omega, \kappa \gg \gamma, g$) and further uses that $U \approx 1$ and $\mathcal{L}_0 = \mathcal{D}(\hat{\zeta}_+)$, $\mathcal{K}_{\text{opt}}\hat{\rho} = \gamma\hat{\zeta}_+\hat{\rho}\hat{\zeta}_-$. We obtain

$$\tilde{N}, \tilde{D}, N = -(e^{-\gamma\tau'} - 1)\tfrac{\tilde{C}}{1-\tilde{C}}(e^{-\tau\gamma\tilde{C}} - e^{-\tau\gamma}), \tag{H52}$$

$$D = -(e^{-\gamma\tau'} - 1)\tfrac{\tilde{C}}{1+\tilde{C}}(e^{-\gamma(1+\tilde{C})\tau} + 1), \tag{H53}$$

and

$$\tilde{E} = 1, \tag{H54}$$

$$E = \frac{1+\tilde{C}}{1-\tilde{C}} \times \frac{e^{-\gamma\tau\tilde{C}} - e^{-\gamma\tau}}{1 - e^{-\gamma(1+\tilde{C})\tau}}. \tag{H55}$$

Figure 9 shows the good agreement between analytics and the numerical results (computed using Qutip [56,57]) for intermediate and large times. Only for small times <10 ns, a small discrepancy is noticeable. In the short-time regime, all N's and D's converge to the same values, making it impractical to evaluate the efficiencies. However, in the more relevant time frame, where E and P_1 reach their maxima, the analytical approach remains effective.

APPENDIX I: IMPACT OF DECOHERENCE

We now consider additional dissipative effects beyond spontaneous emission that may degrade the performance of the source. In particular, we focus here on two mechanisms arising from finite temperature T: thermal noise and pure dephasing.

1. Influence of thermal effects

At finite temperature T, the thermal photon occupation number in the cavity will be $\bar{n} = 1/[\exp(\hbar\omega_c\beta) - 1]$, where $\beta = 1/k_B T$. This arises from the coupling to a thermal bath, described by the following modification of the Lindblad term in the cavity dynamics: $\mathcal{D}(\hat{X}) \to \bar{n}\mathcal{D}(\hat{X}^\dagger) + (\bar{n}+1)\mathcal{D}(\hat{X})$.

The most important consequence is that we must now consider that the initial state of the cavity is the thermal state $\hat{\rho}_T \equiv \sum_{n=0}^{\infty} \exp(-n\hbar\omega_c\beta)|n\rangle\langle n|/[1 - \exp(-\hbar\omega_c\beta)]$. Thermal effects on the population of the emitter and free-space emission can be neglected due to the high visible frequencies yielding negligible thermal occupation numbers. Figure 10 shows the effect of thermal noise on the efficiency, $P_{\max}$, and the indistinguishability I. We can pinpoint a critical temperature below which the dynamics is not affected by thermal occupation and above which there is a sharp decline of both $P_{\max}$ and I due to the rate associated with the thermal noise $\kappa\bar{n}$ becoming important, i.e., at least 10% of the spontaneous emission rate γ. We can estimate the critical temperature $T_{\text{crit}} = \hbar\omega_c/[k_B \ln(1 + 10\kappa/\gamma)]$ by equating these two rates. For our reference value $\omega_c/2\pi \approx 5.12$ THz the system is largely unaffected up to temperatures of $T = 45$ K, enabling optimal operation under standard helium cooling conditions.

2. Influence of pure dephasing

Another important mechanism that typically limits the performance of single-photon emitters is pure dephasing of the quantum emitter. In the dressed-state basis, pure dephasing translates into a combination of dephasing, pumping, and decay processes, described by the replacement $\frac{\Lambda}{2}\mathcal{D}(\hat{\sigma}_z) \to \frac{1}{2}\mathcal{D}(\sqrt{\Lambda_z}\hat{\zeta}_z - \sqrt{\Lambda_-}\hat{\zeta}_- - \sqrt{\Lambda_+}\hat{\zeta}_+)$, where $\Lambda_\pm = 4\Lambda c^2 s^2$ and $\Lambda_z = \Lambda(s^2 - c^2)^2$, respectively. The impact of pure dephasing in the performance of the source is shown in Fig. 11, where one sees that efficiency and indistinguishability are impacted at different thresholds (especially if $g \ll \kappa$). In particular, indistinguishability I is more sensitive and begins to degrade at lower values of Λ than the efficiency $P_{\max}$.

The lower impact on efficiency can be explained by decomposing the pure-dephasing Lindblad term into three separate Lindblad channels (under a rotating-wave approximation) and noting the fact that the $\mathcal{D}(\hat{\zeta}_z)$ term, when added to $\mathcal{L}_{\text{adb}}$, has no effect on $P_1(\tau)$ as given by Eq. (1). Defining a critical dephasing rate for P_1 as the point where the remaining pure dephasing terms reach $\Lambda_\pm = 0.0081\gamma_+$ yields $\Lambda_{\text{crit}}^{(1)} = 0.0081\gamma c^4/(4c^2 s^2)$. Here, the prefactor is motivated by the

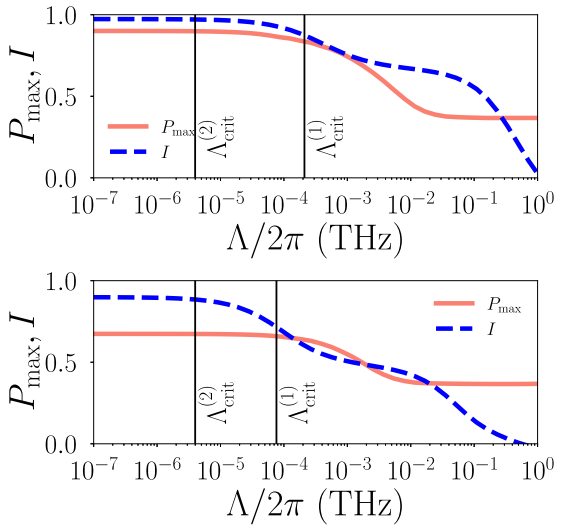


FIG. 11. Numerical results for maximum single-photon detection probability $P_{\max}$ (solid red) and indistinguishability I (dashed blue) as a function of the pure dephasing rate Λ for the parameter set $\{\chi, \kappa, \gamma, \Omega, \Omega_R\}/2\pi = \{12.5, 0.974, 39.78 \times 10^{-3}, 0.2, 5116\}$ GHz (top) and $\{\chi, \kappa, \gamma, \Omega, \Omega_R\}/2\pi = \{4, 3.5, 39.78 \times 10^{-3}, 0.2, 3078\}$ GHz (bottom). The black vertical lines represent the critical value Λ_{crit}, where the pure dephasing is estimated to begin to dominate. For the plot with $\omega_c/2\pi = 3078$ GHz, the indistinguishability is evaluated at $t = 0.95$ ns (maximum of E in Fig. 2).

prior observation that the γ_- term started to matter once $h \geqslant 0.3$, corresponding to $\gamma_-/\gamma_+ = h^4 = 0.0081$.

In contrast, the indistinguishability I is directly affected by the $\mathcal{D}(\hat{\xi}_z)$ term, which is the dominant one in the off-resonant limit. As a result, the adverse effect on the indistinguishability becomes important at much lower dephasing rates than those affecting the single-photon probability P_1. We define a second critical point where pure dephasing rate becomes comparable to the repumping rate γ_+ and influences the indistinguishability as $\Lambda^{(2)}_{\text{crit}} = 0.1\gamma c^4/(s^2 - c^2)^2$. For the parameters considered here, this means that dephasing rates should be below 0.2 GHz to preserve single-photon probability, and below 4 MHz to maintain high indistinguishability.

APPENDIX J: COMPARISON WITH SPONTANEOUS PARAMETRIC DOWN-CONVERSION SOURCES

The main difference between our proposal and SPDCs lies in their fundamental nature: While here we propose a deterministic source, SPDC-based sources are intrinsically probabilistic and generate photon pairs with a distribution over photon-number states. Consequently, detection of an idler photon does not guarantee single-photon emission in the signal mode, and multiphoton contributions are unavoidable [35]. The probability of generating a single photon per pulse is inherently limited to at most 25% (two-mode squeezed state in the limit of unity average photon number). That probability can, theoretically, be improved up to 100% using resource-demanding filtering and multiplexing techniques [58,59]. Experimentally, reported single-photon probabilities are typically on the order of 4%–5% without multiplexing [47,48] and can reach up to 67% with multiplexing strategies [48].

In the THz regime, the only relevant demonstration to our knowledge [10] should, in principle, approach the 25% limit given their reported parametric gain of approximately 0.9. In contrast, our scheme yields single-photon probabilities in the range $P_1 = 65\%$–92% without multiplexing. In the red-detuned regime, emission is fundamentally deterministic, while in the blue-detuned regime it is effectively deterministic due to the slower repumping dynamics relative to the emission process.

Regarding heralding efficiency, reported values in SPDC systems range from approximately 20% in unoptimized configurations [47] up to 97.7% with multiplexing [48]. Our scheme achieves comparable effective efficiencies in the absence of multiplexing.

Regarding purity, state-of-the-art deterministic single-photon sources in the optical domain report indistinguishability values in the range of approximately 74%–99% [35,48]. In our work, the blue-detuned regime yields values of approximately 68%–88%, while the red-detuned regime approaches unity due to suppression of repumping-induced mixing.

[1] I. A. Walmsley, Quantum optics: Science and technology in a new light, Science **348**, 525 (2015).
[2] I. Aharonovich, D. Englund, and M. Toth, Solid-state single-photon emitters, Nat. Photonics **10**, 631 (2016).
[3] A. González-Tudela, A. Reiserer, J. J. García-Ripoll, and F. J. García-Vidal, Light–matter interactions in quantum nanophotonic devices, Nat. Rev. Phys. **6**, 166 (2024).
[4] P. Lodahl, S. Mahmoodian, and S. Stobbe, Interfacing single photons and single quantum dots with photonic nanostructures, Rev. Mod. Phys. **87**, 347 (2015).
[5] A. Blais, A. L. Grimsmo, S. M. Girvin, and A. Wallraff, Circuit quantum electrodynamics, Rev. Mod. Phys. **93**, 025005 (2021).
[6] C. Toninelli, I. Gerhardt, A. S. Clark, A. Reserbat-Plantey, S. Götzinger, Z. Ristanović, M. Colautti, P. Lombardi, K. D. Major, I. Deperasińska, W. H. Pernice, F. H. L. Koppens, B. Kozankiewicz, A. Gourdon, V. Sandoghdar, and M. Orrit, Single organic molecules for photonic quantum technologies, Nat. Mater. **20**, 1615 (2021).
[7] M. Tonouchi, Cutting-edge terahertz technology, Nat. Photonics **1**, 97 (2007).
[8] X. C. Zhang, A. Shkurinov, and Y. Zhang, Extreme terahertz science, Nat. Photonics **11**, 16 (2017).
[9] Y. Todorov, S. Dhillon, and J. Mangeney, THz quantum gap: Exploring potential approaches for generating and detecting non-classical states of THz light, Nanophotonics **13**, 1681 (2024).
[10] A. A. Leontyev, K. A. Kuznetsov, P. A. Prudkovskii, D. A. Safronenkov, and G. Kh. Kitaeva, Direct measurement of the

correlation function of optical–terahertz biphotons, JETP Lett. **114**, 565 (2021).
[11] J. del Pino, F. J. Garcia-Vidal, and J. Feist, Exploiting vibrational strong coupling to make an optical parametric oscillator out of a Raman laser, Phys. Rev. Lett. **117**, 277401 (2016).
[12] J. Iles-Smith, M. K. Svendsen, A. Rubio, M. Wubs, and N. Stenger, On-demand heralded MIR single-photon source using a cascaded quantum system, Sci. Adv. **11**, eadr9239 (2025).
[13] V. Y. Shishkov, O. Kotov, D. Urbonas, L. A. Rozema, F. J. Garcia-Vidal, J. Feist, and A. V. Zasedatelev, Entangled polariton states in the visible and mid-infrared spectral ranges, arXiv:2508.10809.
[14] O. V. Kibis, G. Y. Slepyan, S. A. Maksimenko, and A. Hoffmann, Matter coupling to strong electromagnetic fields in two-level quantum systems with broken inversion symmetry, Phys. Rev. Lett. **102**, 023601 (2009).
[15] I. G. Savenko, O. V. Kibis, and I. A. Shelykh, Asymmetric quantum dot in a microcavity as a nonlinear optical element, Phys. Rev. A **85**, 053818 (2012).
[16] N. Shammah, C. C. Phillips, and S. De Liberato, Terahertz emission from ac Stark-split asymmetric intersubband transitions, Phys. Rev. B **89**, 235309 (2014).
[17] I. Y. Chestnov, V. A. Shahnazaryan, A. P. Alodjants, and I. A. Shelykh, Terahertz lasing in ensemble of asymmetric quantum dots, ACS Photonics **4**, 2726 (2017).
[18] S. De Liberato, Lasing from dressed dots, Nat. Photonics **12**, 4 (2018).
[19] R. Pompe, M. Hensen, M. Otten, S. K. Gray, and W. Pfeiffer, Pure dephasing induced single-photon parametric down-conversion in a strongly coupled plasmon-exciton system, Phys. Rev. B **108**, 115432 (2023).
[20] C. Groiseau, A. I. Fernández-Domínguez, D. Martín-Cano, and C. S. Muñoz, Single-photon source over the terahertz regime, PRX Quantum **5**, 010312 (2024).
[21] B. E. Cole, J. B. Williams, B. T. King, M. S. Sherwin, and C. R. Stanley, Coherent manipulation of semiconductor quantum bits with terahertz radiation, Nature (London) **410**, 60 (2001).
[22] L. Sapienza, M. Davanço, A. Badolato, and K. Srinivasan, Nanoscale optical positioning of single quantum dots for bright and pure single-photon emission, Nat. Commun. **6**, 7833 (2015).
[23] S. Liu, K. Srinivasan, and J. Liu, Nanoscale positioning approaches for integrating single solid-state quantum emitters with photonic nanostructures, Laser Photonics Rev. **15**, 2100223 (2021).
[24] H. S. Kim, A. A. Khan, J.-Y. Park, S. Lee, and Y. H. Ahn, Mechanical control of polaritonic states in lead halide perovskite phonons strongly coupled in THz microcavity, J. Phys. Chem. Lett. **14**, 10318 (2023).
[25] J. Zhang and D. Grischkowsky, Terahertz time-domain spectroscopy study of silica aerogels and adsorbed molecular vapors, J. Phys. Chem. B **108**, 18590 (2004).
[26] COMSOL Multiphysics Reference Manual.
[27] S. Foteinopoulou, G. C. R. Devarapu, G. S. Subramania, S. Krishna, and D. Wasserman, Phonon-polaritonics: Enabling powerful capabilities for infrared photonics, Nanophotonics **8**, 2129 (2018).
[28] B. Gurlek, V. Sandoghdar, and D. Martín-Cano, Manipulation of quenching in nanoantenna–emitter systems enabled by external detuned cavities: A path to enhance strong-coupling, ACS Photonics **5**, 456 (2018).
[29] C. S. Muñoz, F. P. Laussy, E. d. Valle, C. Tejedor, and A. González-Tudela, Filtering multiphoton emission from state-of-the-art cavity quantum electrodynamics, Optica **5**, 14 (2018).
[30] $\hat{\sigma}_\pm = cs\hat{\zeta}_z + s^2\hat{\zeta}_\pm - c^2\hat{\zeta}_\mp$ and $\hat{\sigma}_z = (s^2 - c^2)\hat{\zeta}_z - 2cs(\hat{\zeta}_+ + \hat{\zeta}_-)$.
[31] A. Ridolfo, M. Leib, S. Savasta, and M. J. Hartmann, Photon blockade in the ultrastrong coupling regime, Phys. Rev. Lett. **109**, 193602 (2012).
[32] C. Gonzalez-Ballestero, Tutorial: Projector approach to master equations for open quantum systems, Quantum **8**, 1454 (2024).
[33] In this derivation, we discarded the coherent part, which only consists in an energy shift inconsequential for P since $[\hat{\zeta}_+\hat{\zeta}_-, |\pm\rangle\langle\pm|] = 0$.
[34] P. Senellart, G. Solomon, and A. White, High-performance semiconductor quantum-dot single-photon sources, Nat. Nanotechnol. **12**, 1026 (2017).
[35] M. Esmann, S. C. Wein, and C. Antón-Solanas, Solid-state single-photon sources: Recent advances for novel quantum materials, Adv. Funct. Mater. **34**, 2315936 (2024).
[36] I. A. Ostapenko, G. Hönig, C. Kindel, S. Rodt, A. Strittmatter, A. Hoffmann, and D. Bimberg, Large internal dipole moment in InGaN/GaN quantum dots, Appl. Phys. Lett. **97**, 063103 (2010).
[37] C. Kindel, G. Callsen, S. Kako, T. Kawano, H. Oishi, G. Hönig, A. Schliwa, A. Hoffmann, and Y. Arakawa, Spectral diffusion in nitride quantum dots: Emission energy dependent linewidths broadening via giant built-in dipole moments, Phys. Status Solidi RRL **8**, 408 (2014).
[38] Y. Ossia, A. Levi, Y. E. Panfil, S. Koley, E. Scharf, N. Chefetz, S. Remennik, A. Vakahi, and U. Banin, Electric-field-induced colour switching in colloidal quantum dot molecules at room temperature, Nat. Mater. **22**, 1210 (2023).
[39] K. Müller, A. Bechtold, C. Ruppert, M. Zecherle, G. Reithmaier, M. Bichler, H. J. Krenner, G. Abstreiter, A. W. Holleitner, J. M. Villas-Boas, M. Betz, and J. J. Finley, Electrical control of interdot electron tunneling in a double InGaAs quantum-dot nanostructure, Phys. Rev. Lett. **108**, 197402 (2012).
[40] L. Wang, A. Rastelli, S. Kiravittaya, M. Benyoucef, and O. G. Schmidt, Self-assembled quantum dot molecules, Adv. Mater. **21**, 2601 (2009).
[41] B. Lv, T. Zhu, Y. Tang, Y. Lv, C. Zhang, X. Wang, D. Shu, and M. Xiao, Probing permanent dipole moments and removing exciton fine structures in single perovskite nanocrystals by an electric field, Phys. Rev. Lett. **126**, 197403 (2021).
[42] H. Kim, T. C. Shen, K. Roy-Choudhury, G. S. Solomon, and E. Waks, Resonant interactions between a Mollow triplet sideband and a strongly coupled cavity, Phys. Rev. Lett. **113**, 027403 (2014).
[43] K. Boos, S. K. Kim, T. Bracht, F. Sbresny, J. M. Kaspari, M. Cygorek, H. Riedl, F. W. Bopp, W. Rauhaus, C. Calcagno, J. J. Finley, D. E. Reiter, and K. Müller, Signatures of dynamically dressed states, Phys. Rev. Lett. **132**, 053602 (2024).
[44] S. Komiyama, O. Astafiev, V. Antonov, T. Kutsuwa, and H. Hirai, A single-photon detector in the far-infrared range, Nature (London) **403**, 405 (2000).

[45] Z. An, T. Ueda, S. Komiyama, and K. Hirakawa, Metastable excited states of a closed quantum dot with high sensitivity to infrared photons, Phys. Rev. B **75**, 085417 (2007).

[46] P. M. Echternach, B. J. Pepper, T. Reck, and C. M. Bradford, Single photon detection of 1.5 THz radiation with the quantum capacitance detector, Nat. Astron. **2**, 90 (2018).

[47] J. N. Tinsley, M. I. Molodtsov, R. Prevedel, D. Wartmann, J. Espigulé-Pons, M. Lauwers, and A. Vaziri, Direct detection of a single photon by humans, Nat. Commun. **7**, 12172 (2016).

[48] F. Kaneda and P. G. Kwiat, High-efficiency single-photon generation via large-scale active time multiplexing, Sci. Adv. **5**, eaaw8586 (2019).

[49] M. Bock, A. Lenhard, C. Chunnilall, and C. Becher, Highly efficient heralded single-photon source for telecom wavelengths based on a PPLN waveguide, Opt. Express **24**, 23992 (2016).

[50] S. Hughes, S. Franke, C. Gustin, M. Kamandar Dezfouli, A. Knorr, and M. Richter, Theory and limits of on-demand single-photon sources using plasmonic resonators: A quantized quasinormal mode approach, ACS Photonics **6**, 2168 (2019).

[51] R. M. Corless, G. H. Gonnet, D. E. G. Hare, D. J. Jeffrey, and D. E. Knuth, On the LambertW function, Adv. Comput. Math. **5**, 329 (1996).

[52] B. J. Sussman, J. G. Underwood, R. Lausten, M. Y. Ivanov, and A. Stolow, Quantum control via the dynamic Stark effect: Application to switched rotational wave packets and molecular axis alignment, Phys. Rev. A **73**, 053403 (2006).

[53] A. Goban, S. Minemoto, and H. Sakai, Laser-field-free molecular orientation, Phys. Rev. Lett. **101**, 013001 (2008).

[54] E. Meyer-Scott, N. Montaut, J. Tiedau, L. Sansoni, H. Herrmann, T. J. Bartley, and C. Silberhorn, Limits on the heralding efficiencies and spectral purities of spectrally filtered single photons from photon-pair sources, Phys. Rev. A **95**, 061803 (2017).

[55] H. E. Guilbert and D. J. Gauthier, Enhancing heralding efficiency and biphoton rate in type-I spontaneous parametric down-conversion, IEEE J. Sel. Top. Quantum Electron. **21**, 215 (2015).

[56] J. R. Johansson, P. D. Nation, and F. Nori, QuTiP: An open-source Python framework for the dynamics of open quantum systems, Comput. Phys. Commun. **183**, 1760 (2012).

[57] J. R. Johansson, P. D. Nation, and F. Nori, QuTiP 2: A Python framework for the dynamics of open quantum systems, Comput. Phys. Commun. **184**, 1234 (2013).

[58] Y. Zhang, M. Jiang, Z. Wu, Q. Yang, Y. Men, L. Cheng, P. Liang, R. Hu, T. Jia, Z. Sun, and D. Feng, Hyperfine-induced electron-spin dephasing in negatively charged colloidal quantum dots: A survey of size dependence, J. Phys. Chem. Lett. **12**, 9481 (2021).

[59] A. Christ and C. Silberhorn, Limits on the deterministic creation of pure single-photon states using parametric down-conversion, Phys. Rev. A **85**, 023829 (2012).